Numerical modelling of the upper-mantle anisotropy beneath a migrating strike-slip plate boundary: the San Andreas Fault system

Mickaël Bonnin, Andrea Tommasi, Riad Hassani, Sébastien Chevrot, James Wookey, Guilhem Barruol

Geophysical Journal International

Geophys. J. Int. (2012) **191,** 436–458 doi: 10.1111/j.1365-246X.2012.05650.x

Numerical modelling of the upper-mantle anisotropy beneath a migrating strike-slip plate boundary: the San Andreas Fault system

Mickaël Bonnin,[1] Andréa Tommasi,[1] Riad Hassani,[2] Sébastien Chevrot,[3] James Wookey[4] and Guilhem Barruol[5]

[1] *Géosciences Montpellier, UMR* 5243*, CNRS & Université de Montpellier* 2*, Place E. Bataillon, F-*34095 *Montpellier Cedex* 5*, France. E-mail: bonnin@gm.univ-montp2.fr*

[2] *Géoazur, UMR* 7329*, CNRS & Université de Nice – Sophia Antipolis, F-*06560 *Valbonne, France*

[3] *Institut de Recherche en Astrophysique et Planétologie, CNRS, UMR* 5277*, Observatoire Midi-Pyrénées, Université Paul Sabatier, Toulouse* 14 *Avenue Edouard Belin, F-*31400 *Toulouse, France*

[4] *School of Earth Sciences, University of Bristol, Wills Memorial Building, Queens Road, Bristol BS*8 *1RJ, UK*

[5] *Géosciences Réunion, Université de la Réunion, IPGP & CNRS,* 15 *Avenue R. Cassin BP* 7151*, F-*97715 *Saint Denis Cedex* 9*, La Réunion, France*

Accepted 2012 August 14. Received 2012 August 13; in original form 2012 March 8

SUMMARY

We performed forward modelling of seismic anisotropy beneath a migrating strike-slip plate boundary to: (1) test if such a geodynamic context might explain teleseismic shear wave splitting data in the vicinity of the central part of the San Andreas Fault and (2) constrain the power of such data to unravel vertical and lateral variations in deformation patterns in the upper mantle. The modelling involves five steps: (1) thermomechanical modelling, using a finite-element code, of the deformation field, (2) viscoplastic self-consistent modelling of the resulting olivine and pyroxene crystal preferred orientations, (3) calculation of the elasticity tensors for different domains of the finite elements (FEs) model, (4) forward modelling of seismic wave propagation through the model using ray theory, finite-frequency theory and a full-wave approach and (5) performing splitting measurements on the synthetic seismograms. *SKS* splitting data in central California are best fitted by a model with a hotter geotherm within 60 km of the plate boundary accounting for the opening of an asthenospheric window due to the northward migration of the Mendocino Triple Junction. The westward motion of the plate boundary cannot however explain the rotation of fast polarization directions east of the San Andreas Fault in central California. Comparison between modelled and measured individual shear wave splitting also implies that the homogeneity of the two-layer models accounting for the observations in the vicinity of the San Andreas Fault indicates a sharp transition between lithospheric and asthenospheric deformations beneath this plate boundary. The ability of different synthetic approaches to localize horizontally and vertically the plate boundary-related deformation differs significantly. Splitting in ray theory synthetics closely follow variations in olivine crystallographic preferred orientations in the model. In contrast, splitting analysis on full-wave synthetics, which should be more representative of actual long-period *SKS* waves, results in smooth apparent lateral variations of anisotropy; the exact location and width of the plate boundary may only be retrieved by comparing fast-polarization profiles obtained using a multichannel analysis on waves with different periods.

Key words: Seismic anisotropy; Continental tectonics: strike-slip and transform; Dynamics of lithosphere and mantle; Rheology: mantle; North America.

1 INTRODUCTION

Plate boundaries localize most of the deformation at the Earth's surface. They are also privileged regions of interaction between brittle and ductile levels of the crust, or between the plates and the convecting mantle. They are therefore key zones for understanding the dynamics of the deep Earth and for unravelling the depth extent of plate tectonics processes. Due to their relatively simple geometry: they probably crosscut the entire lithosphere preserving similar kinematics at all depths (Vauchez *et al.* 2012), strike-slip plate boundaries are ideal locations for characterizing the changes in the lateral distribution of deformation with depth. However, although the deformation at various crustal levels may be accessed by direct surface observations, this is not the case for the

underlying mantle, which is, in most cases, the highest strength layer in the system. Upper-mantle deformation can be resolved through indirect observations, in particular by analysing the splitting of vertically propagating shear waves (mainly core phases like *SKS*). This technique provides constraints on the strain-induced orientations of olivine crystals in the upper mantle with a lateral resolution of the order of tens of kilometres (Silver 1996; Savage 1999). However, because of their almost vertical propagation, core shear waves have very limited vertical resolution. Consequently, despite the combination of a large number of field studies, geophysical observations, numerical and experimental modelling, the vertical distribution of deformation beneath strike-slip plate boundaries remains poorly constrained and many questions remain open. Does the strike-slip deformation affect the whole lithosphere? Do these faults reach and penetrate the asthenosphere? To which level are the lithosphere and asthenosphere mechanically coupled? How strongly localized is strain at different depth levels beneath such plate boundaries?

In an absolute plate motion (APM) reference frame, like the 'HS3-NUVEL 1A' model (Gripp & Gordon 2002), not only the plates, but also plate boundaries may move relative to the deeper mantle through geological times. Horizontal displacement of the plates (and plate boundaries) relative to the deep mantle are expected to induce shearing in the less-viscous asthenosphere, as classically proposed for explaining anisotropy beneath oceans (e.g. Hess 1964; Tommasi 1998; Wolfe & Solomon 1998; Harmon *et al.* 2004; Fontaine *et al.* 2007). This deformation may potentially interact with the overlying deformation produced by strike-slip motion at the plate boundary. Interactions between these two deformation processes may result in complex anisotropic patterns beneath plate boundaries, such as several anisotropic layers or smoothly vertically or laterally varying anisotropies that are difficult to detect using teleseismic waves. Despite this hypothetical incidence on the anisotropy pattern, the migration of strike-slip plate boundaries is still largely ignored in *SKS* splitting interpretations.

To address these questions and to provide better interpretations of *SKS* splitting observations, we focus on the San Andreas Fault system and, more particularly, on its central part, which has been extensively studied during the last two decades (Savage & Silver 1993; Ozalaybey & Savage 1994, 1995; Silver & Savage 1994; Hartog & Schwartz 2000, 2001; Polet & Kanamori 2002; Bonnin *et al.* 2010). This segment of the San Andreas Plate boundary is characterized by anisotropy patterns often interpreted with a model involving the presence of two distinct anisotropic layers (Savage & Silver 1993; Silver & Savage 1994; Ozalaybey & Savage 1995; Hartog & Schwartz 2001; Bonnin *et al.* 2010). The upper layer, which is likely located in the lithosphere and spatially related to the transform plate boundary, is characterized by polarization of the fast shear wave parallel to the strike of the San Andreas Fault. The lower layer, interpreted as asthenospheric, is characterized by E–W polarization of the fast shear wave, a pattern ubiquitously observed through most of California (e.g. Liu *et al.* 1995; Polet & Kanamori 2002; Monteiller & Chevrot 2011). Many interpretations were proposed to explain this E–W fast-polarization direction. Ozalaybey & Savage (1995) proposed that it is related to mantle flow filling the slab window caused by the northward migration of the Mendocino Triple Junction. Hartog & Schwartz (2000) invoked frozen-in fabrics associated to the subduction of the old Gorda Plate. Polet & Kanamori (2002) proposed a mix of old subduction processes and recent tectonic activities. Finally, Silver & Holt (2002) invoked a combination of large-scale eastward mantle flow in the asthenosphere in relation with the Farallon slab sinking and westward displacement of the North America lithosphere. As fast shear wave polarization directions observed beneath the Pacific Ocean and the Sierra Nevada are subparallel to the APM obtained from 'HS3-NUVEL 1A' model (Gripp & Gordon 2002) for the Pacific and North America plates, respectively, Bonnin *et al.* (2010) proposed that the anisotropy in this layer is related to simple shear in the asthenosphere by the motion of the lithospheric plates relative to a 'passive' deep mantle. They also suggested the smooth rotation of the directions of polarization observed in the Great Valley area to be caused by the reorientation of the crystallographic fabrics in the asthenosphere in response to the progressive westward displacement of the North America plate above the old Pacific asthenosphere.

To study the deformation and anisotropy beneath a migrating strike-slip plate boundary like the San Andreas Fault system, we follow a 3-D numerical modelling approach similar to the one developed by Savage *et al.* (2007). It involves five steps: (1) We model the deformation of a strike-slip lithospheric plate boundary moving above a passive asthenosphere using a 3-D finite element (FE) thermomechanical code to obtain the velocity field and associated strain rates. (2) Based on the modelled velocity gradient fields, we calculate for each element of the model, using a viscoplastic self-consistent approach, the development of crystallographic fabrics of olivine and enstatite. (3) Similarly, we also calculate the corresponding elastic properties of the 70 per cent olivine–30 per cent enstatite aggregates. (4) We then compute synthetic *SKS* waves that propagate in the anisotropic medium defined by these complex 3-D structures. (5) We analyse the synthetic seismograms of *SKS* waves to determine the anisotropy parameters that will be compared to those obtained from real seismological records in central California.

2 METHODS

2.1 Thermomechanical modelling

We use the FE code 'ADELI 3D' (Hassani *et al.* 1997; Chéry *et al.* 2001, 2004) to model the thermomechanical behaviour of a strike-slip plate boundary moving over a 'passive' deep mantle. This code solves for the quasi-static mechanical behaviour of the lithosphere using an explicit scheme based on the Dynamic Relaxation Method (Cundall & Board 1988). In this study we focus on mantle deformation, but elasto-viscoplastic crustal layer is added on the top of the model. This allows us to introduce a zone of weakness in the brittle crust to localize the deformation on the surface of the plate boundary, without imposing any *a priori* heterogeneity in the lithospheric or asthenospheric mantle. The deformation is thus allowed to develop freely in the mantle.

The modelled domain (Fig. 1) is 210 km large in a direction normal to the plate boundary, 20 km wide parallel to the plate boundary and 550 km thick. It is meshed with 2-km-wide tetrahedral blocks. On the top of the model, two 30-km-thick and 100-km-large blocks account for the Pacific oceanic mafic crust to the left and for the continental North America felsic crust to the right. These crustal blocks are separated by a 10-km-large felsic domain in which the internal friction angle has been reduced to 10° instead of 15°. This drop of the friction angle follows previous studies on the behaviour of the San Andreas Fault (e.g. Chéry *et al.* 2001) and represents the weakening resulting from damage in the brittle crust within the San Andreas Fault zone. Two homogeneous peridotitic blocks, representing the lithospheric and sublithospheric mantle, compose the remaining of the model. The positions of the different discontinuities are given in Table 1. Crustal blocks deform

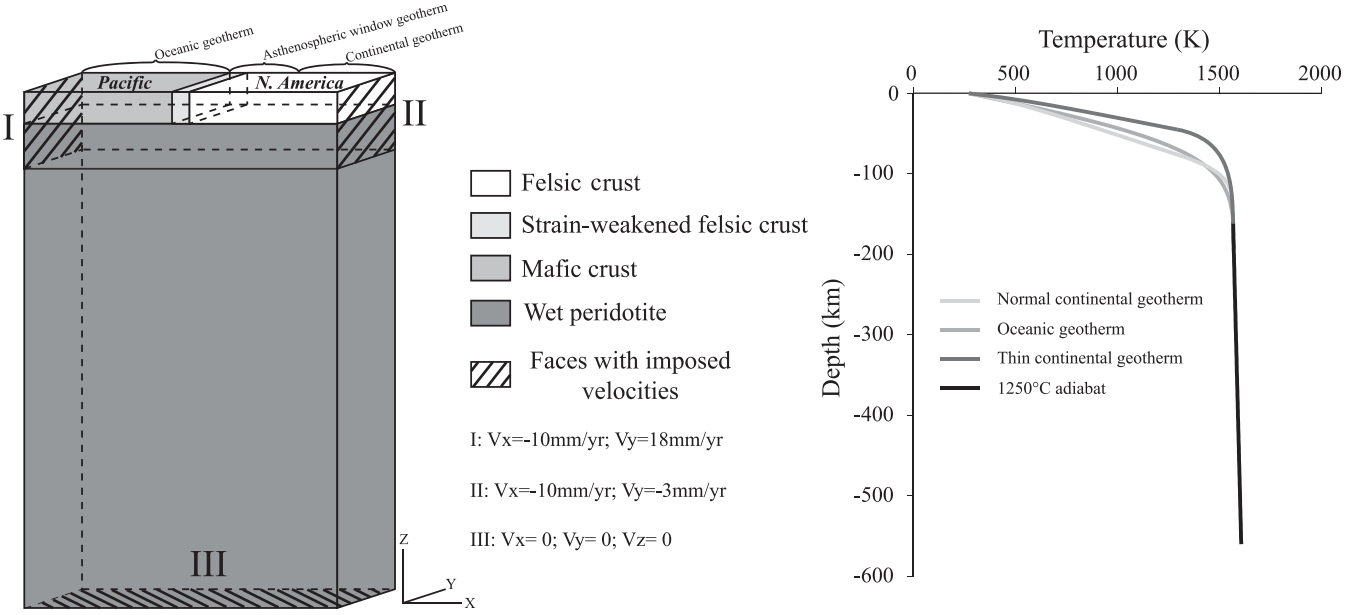

Figure 1. Geometry and boundary conditions of the thermomechanical model and the initial geotherms used in the various domains of the model. Grey levels indicate domains with different compositions. The Pacific absolute plate velocity was imposed on face (I); North America absolute plate velocity was imposed on face (II). The bottom of the model (face III) is fixed.

Table 1. Localization of the different interfaces.

	X (km)	*Y* (km)	*Z* (km)
'Oceanic' crust	0–100	0–20	0 to –30
Fault zone	100–110	0–20	0 to –30
'Continental' crust	110–210	0–20	0 to –30
'Lithospheric' mantle	0–210	0–20	−30 to −80
'Asthenospheric' mantle	0–210	0–20	−80 to −550

either elasto-plastically or viscoelastically depending on which behaviour results in the smaller work. The plastic (frictional) behaviour is described by a Druker–Prager yield criterion and the viscous deformation follows a power-law relationship with an exponential dependence on temperature. Mantle blocks are viscoelastic and follow a power law with both temperature and pressure dependences. Rheological parameters for all domains are given in Table 2.

Several initial temperature fields have been tested but only two end-member cases will be presented here. The first one, called 'TSAFM' has a geotherm calculated using a half-space cooling model for a 50-Myr-old oceanic lithosphere on the Pacific side and by a 'normal' continental geotherm corresponding to a lithosphere thickness of 100 km (Turcotte & Schubert 1982) in the remaining of the model (Fig. 1). In the second one, called 'TDT60', a hotter geotherm representing a 50-km-thick continental lithosphere is imposed in a domain 60 km large to the right of the plate boundary to account for the thermal perturbation caused by the opening of the asthenospheric window due to the northward migration of the Mendocino Triple Junction. Geophysical data (Lachenbruch & Sass 1980; Lachenbruch *et al.* 1985; Benz *et al.* 1992; Burdick *et al.* 2008) imply that 'TDT60' represents a more realistic temperature field for the studied region. Comparison between 'TSAFM' and 'TDT60' models allows, however, evaluation of the effect of the initial temperature field on the strain distribution beneath the plate boundary. Models with other initial temperature fields are not discussed as they are less realistic and display deformation fields that do not differ significantly from the two presented here.

Velocity boundary conditions consistent with 'HS3-NUVEL 1A' (Gripp & Gordon 2002) absolute velocities for the Pacific and North America plates are imposed on the uppermost 80 and 100 km of the lateral edges of the Pacific and North America plates, respectively (Fig. 1). To avoid transpressional or transtensional deformations, we however apply similar velocities along the *X* direction for both plates, therefore imposing a pure strike-slip regime. As a consequence, they have directions that slightly differ from the true 'HS3-NUVEL 1A' velocities and can thus not be directly compared to observations in California. Vertical displacements are free on these

Table 2. Physical parameters used in the thermomechanical simulations.

	Quartzite	Dry diabase plg-rich	Dry diabase cpx-rich	Dry dunite
Density (kg m^{-3})	2.7e^3	2.8e^3	2.8e^3	3.3e^3
Young modulus (Pa)	1.e^{11}	1.e^{11}	1.e^{11}	1.e^{11}
Poisson ratio	0.25	0.25	0.25	0.25
Fluidity, γ (Pa^{-n} s^{-1})	1.10e^{-28}	1.20e^{-26}	3.41e^{-28}	7.24e^{-18}
Activation energy Q (kJ mol^{-1} K^{-1})	223	485	445	530
Stress exponent, *n*	3.5	3.5	3.5	3.5
Power-law breakdown stress	–	1000	1000	500
Reference stress, σ_0 (Pa)	–	8.5e^9	8.5e^9	8.5e^9
Reference strain rate, $\dot{\varepsilon}_0$ (s^{-1})	–	8.55e^{11}	8.55e^{11}	8.55e^{11}
Thermal conductivity, k (W m^{-1})	2.7	2.7	2.7	3.5

faces. The bottom of the model is fixed. Lithostatic pressure conditions are applied on the lateral (*YZ*) faces below the domain on which plate velocities are imposed. On the frontal and rear (*XZ*) faces, elements are free to move along the *X* and *Y* directions but fixed in the *Z* direction. This ensures a pure strike-slip regime, stabilizing the calculation. All experiments are performed for a duration of 0.5 Myr, which allows us to attain a quasi-steady-state behaviour while keeping calculation times reasonable (several days on a personal computer). It also prevents the development of a strong deformation of the mesh and thus avoids the need to re-mesh the model.

2.2 Crystal preferred orientations

The development of olivine and orthopyroxene crystallographic preferred orientations (CPO) as a function of strain is calculated using a viscoplastic self-consistent (VPSC) model (Lebensohn & Tomé 1993). This model simulates the CPO evolution due to plastic deformation by dislocation glide in a two-phase (70 per cent olivine–30 per cent enstatite) polycrystalline material. In polycrystal plasticity models, CPO evolution is essentially controlled by the imposed deformation, the initial texture (crystal-preferred and, to a lesser extent, shape-preferred orientation) and the active slip systems. The latter not only depend on the mineral structure, but also on the temperature and pressure conditions, which control their relative strength or critical resolved shear stress. To simulate olivine and pyroxene CPO evolution in the lithospheric mantle and asthenosphere, we use, as in previous viscoplastic self-consistent simulations for olivine (Wenk *et al.* 1991; Tommasi *et al.* 2000), slip systems data (Table 3) derived from high-temperature, low-pressure single-crystal deformation experiments (Bai *et al.* 1991). The deformation history is derived from the final velocity gradient field in the mechanical model. We found that for times higher than 300 ka, that is, after the relaxation of elastic stresses, the flow pattern in the mantle does not change significantly, allowing us to calculate the evolution of CPO for times longer than those attained in the thermomechanical model. To reduce calculation times, we avoid calculating the CPO evolution in neighbouring elements with similar deformation histories. Instead, we search over the entire FE model and create velocity gradient tensor 'classes'. Within each class, variations for each of the tensor components are less than 2.5×10^{-15} s^{-1}. This value is chosen depending on the range of strain rates in the model. It is sufficiently small to precisely describe slowly deforming domains but high enough not to over-discretize the domains facing large strain rates. Olivine and enstatite CPO evolution are then calculated for each velocity gradient tensor 'class'. These CPO are then used to compute the aggregate seismic properties based on a Voigt–Reuss–Hill average of the elastic constants of olivine and enstatite at ambient pressure and temperature (Mainprice 1990).

Table 3. Olivine slip systems' critical resolved shear stresses (CRSS) and stress exponents used in VPSC calculations.

Slip systems	CRSS	Stress exponent
(010)[100]	1	3
(001)[100]	1	3
(010)[001]	2	3
(100)[001]	3	3
{011}[100]	4	3
{111}[110]	50	3
{111}[011]	50	3

The calculated CPO and the corresponding stiffness tensors are then tracked back to the final positions of the elements in the model.

2.3 Synthetic *SKS*

To predict the signature of seismic anisotropy in our model and compare it to *SKS* splitting measurements performed in central California, we modelled the propagation of shear waves through the 3-D anisotropic model and analysed the resulting signal to obtain splitting parameters. Synthetic seismograms have been generated using two different approaches. The first one is based on ray theory. The second one is a more general full-waveform approach that accounts for the finite size of *SKS* Fresnel zones, of the order of 100 km for a dominant period of 8 s (e.g. Favier & Chevrot 2003). Full-waveform synthetics are obviously more accurate and can be compared directly to *SKS* splitting observations. In both cases, the calculation of the synthetics starts at a depth of 300 km below which deformation becomes very small. It is also a depth below which very weak anisotropy is both measured and predicted by models that consider the pressure dependence of olivine deformation mechanisms (Mainprice *et al.* 2005).

In the ray theory approach, we assume that the paths are vertical. We consider a profile of receivers spaced by 5 km along the *X* direction. Each 10 km along the ray path, splitting operators are determined using the closest neighbour of the FE elastic tensor grid. The amount of anisotropy, the polarization of the fast *qS* wave and the velocity of the *qS* and *P* waves are calculated by solving the Christoffel equation (e.g. Mainprice 1990). When the variation in the direction of polarization of the fast wave along the ray path is less than 1°, splitting operators are agglomerated, that is, initial direction of polarization is kept and delay times are summed. If variation in the direction of polarization is higher than 1°, a new splitting operator is determined. Once the splitting operators are defined for the entire ray path, they are applied in sequence to an unsplit wavelet with a dominant period of 10 s and initial polarizations varying from 0° to 180° by steps of 10° to generate realistic seismograms and particle motions.

In the full-wave approach, we calculate synthetics using a code developed by Chevrot *et al.* (2004) and Chevrot (2006) based on initial work by Komatitsch & Tromp (1999). In this approach, a planar shear wave propagates vertically in a 400 × 400 × 400 km spectral elements grid (elements are 10 km wide) in which we introduce the elasticity tensors of our FE model aggregates using a nearest neighbour algorithm. The initial polarization of the plane waves varies between 0° and 180° by increments of 20° and the calculations are performed for dominant periods of 5, 8, 10 and 15 s.

2.4 Splitting measurements

We measure splitting parameters using two different methods. The first one is commonly used in *SKS* splitting studies and consists in determining the (ϕ, δt) pair that best minimizes the energy on the transverse component (Silver & Chan 1991). This method is the one used by Bonnin *et al.* (2010) to measure *SKS* splitting in central California. Results obtained for our models can thus be easily compared to their measurements. This method is implemented in the SHEBA program (Teanby *et al.* 2004; Wüstefeld & Bokelmann 2007; Wüstefeld *et al.* 2010), which automatically determines splitting parameters for the entire data set. Variations of splitting parameters as a function of initial polarization of the wave, obtained with this method, may carry information on the vertical

distribution of the anisotropy beneath the receiver (Savage & Silver 1993; Silver & Savage 1994).

The second technique is based on the multichannel approach developed by Chevrot (2000). It considers the whole data set to determine an average value of the splitting parameters beneath each station. Splitting intensity (SI) is measured by projecting the transverse component on the derivative of the radial component. Fitting the azimuthal variation of SI at each station with a 180° periodic sinusoid gives the average splitting parameters. This method gives more stable results for weak or noisy signals (Monteiller & Chevrot 2010).

3 RESULTS

3.1 Thermomechanical model

3.1.1 'TSAFM' model: homogeneous continental geotherm beneath North America

Finite strain and velocity fields after 0.5 Myr (top) and the evolution of finite strain through time along vertical cross-sections on both plates and along the fault (bottom) are presented in Fig. 2. Despite the lower friction angle in the crustal block beneath the fault, strain localization at the plate boundary is weak. The strike-slip motion between the Pacific and the North America plates is dominantly accommodated in the Pacific Plate, which has a slightly hotter geotherm, but is distributed over a large volume. Analysis of the finite strain distribution with depth on the Pacific side at 50 km from the plate boundary (profile B in Fig. 2) shows a homogeneous deformation of the lithosphere. Higher strains characterize the lithosphere–asthenosphere boundary in all profiles, indicating that the velocity gradient between the plates and the deep mantle are essentially accommodated in this layer. Strain distribution in the asthenosphere is asymmetric due to the competing effects of temperature and pressure on mantle viscosity. Lower strains are observed beneath the North America Plate (profile D in Fig. 2) due to the lower absolute plate velocity motion of the plates relative to the fixed deep mantle. At the plate boundary, the strain distribution with depth (profile C in Fig. 2) is more heterogeneous. High strains characterize the crust and the lithosphere–asthenosphere boundary. Strains are much lower in the shallow lithospheric mantle. This low-strain domain corresponds to depths where the continental geotherm is cooler than the oceanic geotherm (Fig. 1). The reduction of the friction angle does result in strain localization in the crust, but then the strike-slip deformation is transferred to the Pacific Plate lithospheric mantle, because of its higher temperatures.

3.1.2 'TDT60' model: hotter geotherm in the North America Plate within 60 km from the fault

This model, characterized by a thinner and hotter lithospheric mantle in the North America Plate within 60 km of the plate boundary, shows a different behaviour, with strain localization beneath the plate boundary (Fig. 3). Analysis of the finite strain distribution in the horizontal section at 70 km depth (profile A in Fig. 3) highlights an asymmetric strain distribution in the lithospheric mantle. Highest finite strains are observed just beneath the fault boundary. Strain decreases abruptly on the Pacific side. The North America Plate records a gradual decrease in finite strain within the hotter geotherm domain and an abrupt reduction at the eastern edge of the asthenospheric window. Strain localization is therefore strongly controlled by the thermal structure of the lithosphere.

Analysis of the horizontal cross-section at 150 km depth (i.e. at asthenospheric depths, profile B in Fig. 3) also shows an important asymmetry in the strain distribution. Finite strain is significantly higher beneath the Pacific Plate. The faster absolute velocity of the Pacific Plate relatively to the North America Plate may explain this difference. High strain is also observed beneath the plate boundary, suggesting that the strike-slip contribution is still present at asthenospheric depths.

The finite strain distribution beneath the Pacific Plate (vertical profile C in Fig. 3) indicates that strain is localized between 100 and 250 km depth with the highest values around 150 km. This is consistent with a horizontal shear zone accommodating asthenospheric deformation by drag by the moving plate and a 'rigid' behaviour of the lithosphere. A similar pattern is observed beneath the North America Plate (vertical profile E in Fig. 3), but the highest strains are at shallower depths (∼100 km) and the shear zone is thinner. Beneath the plate boundary (vertical profile D in Fig. 3), finite strains are up to one order of magnitude higher than in the intraplate profiles. The highest values are in the lithosphere, suggesting that the imposed strike-slip deformation predominates in this domain.

Analysis of the evolution of strain rates through time (Fig. 3 profile C') shows a clear decrease in the rate of evolution, justifying the use of the velocity gradients obtained at the end of the experiment for calculating the CPO evolution for larger time spans. Hereafter we will only present results obtained for the 'TDT60' model, our preferred model, as the absence of strain localization beneath the plate boundary using the 'TSAFM' geotherm does not allow for a description of the vertical distribution of the deformation beneath the fault.

3.2 Crystal-preferred orientations and seismic properties

Evolution of olivine and enstatite CPO were calculated by extrapolating the velocity gradients obtained in the thermomechanical models over 5 Myr. Averaging of the velocity gradients over several time steps allowed avoiding short wavelength variations associated with numerical errors. This 5 Myr duration corresponds to the estimated elapsed time (Titus *et al.* 2007) since the stabilization of the asthenosphere geotherm after the opening of the asthenospheric window associated to the migration of the Mendocino Triple Junction in the central California region 10 Ma (Atwater 1970; Dickinson & Snyder 1979; Dickinson 1997). We assume that the strong deformation associated with this process fully reoriented the olivine CPO and hence resettled the anisotropy in the asthenosphere in the region. 5 Myr may therefore represent a time zero for the development of olivine CPO consistent with the present plate boundary configuration.

To test the influence of pre-existing crystallographic fabrics on the final anisotropy, VPSC calculations have been run for three different initial states (Fig. 4): (1) isotropic 70 per cent olivine–30 per cent enstatite aggregates; (2) aggregates in which olivine [100] axes are oriented in the direction of APM of the North America Plate and [010] axes are vertical and (3) aggregates in which olivine [100] axes are oriented in the direction of APM of the Pacific Plate and [010] axes are vertical. The last two configurations mimic olivine CPO produced by shearing of the asthenosphere by drag beneath a moving plate with the APM of the North America and the Pacific plates, respectively (Tommasi *et al.* 1999).

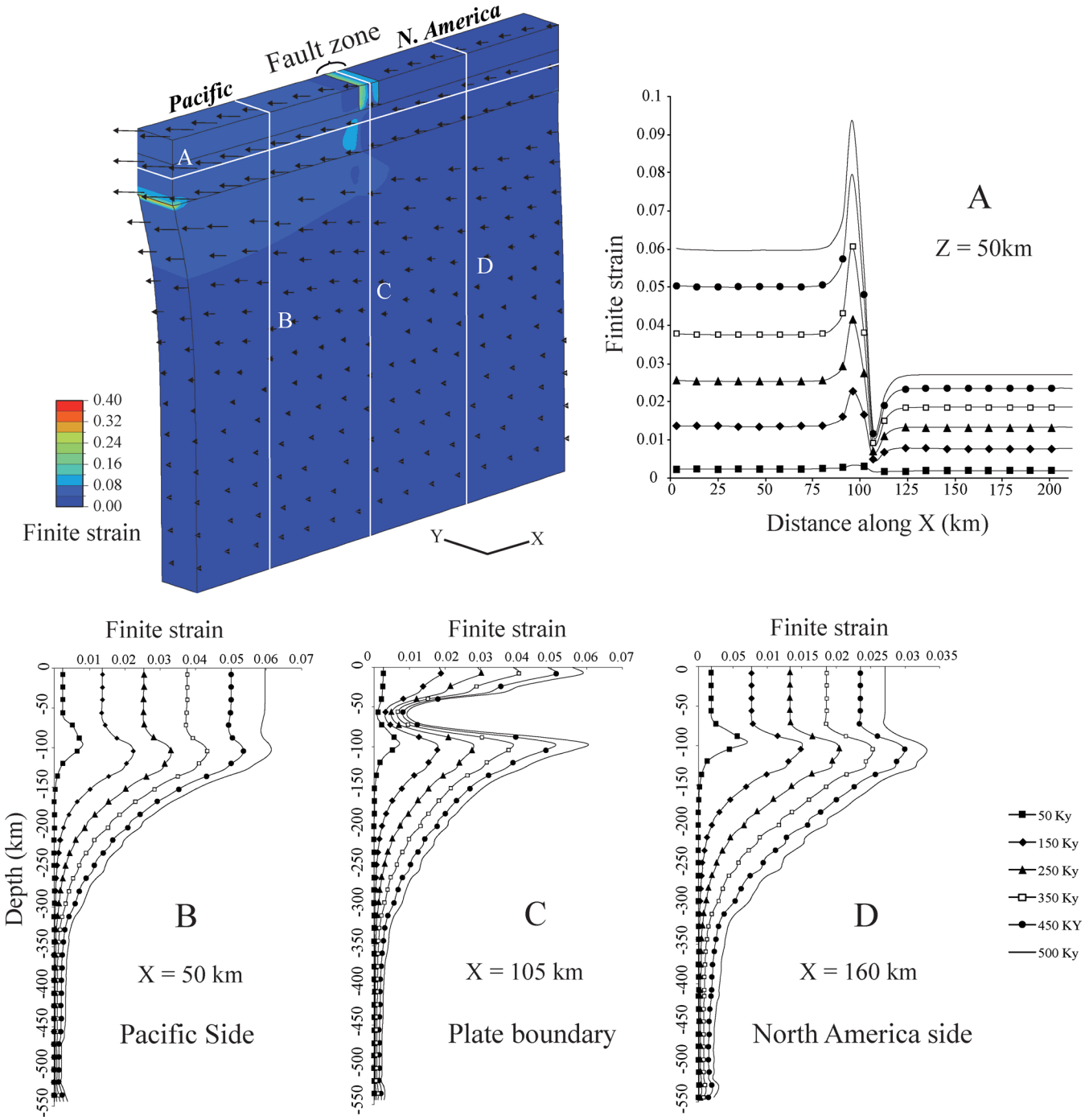

Figure 2. Top left: Finite strain (second invariant) and velocity fields after 0.5 Myr of deformation for a model using the 'TSAFM' initial temperature field, that is, a homogeneous 'normal continental geotherm' for the North America Plate. White lines represent the profiles. Top right: Temporal evolution of the second invariant of the finite strain along a horizontal profile (A) at 50 km depth. Bottom: Temporal evolution of the second invariant of the finite strain along vertical profiles across (B) the Pacific Plate at $X = 50$ km beneath the plate boundary, (C) at $X = 105$ km and (D) across the North America Plate at $X = 160$ km.

3.2.1 Random initial crystallographic fabrics

Olivine CPO and seismic properties characteristic of: (1) the shallow lithospheric mantle beneath the plate boundary; (2) the asthenospheric mantle beneath the Pacific Plate, (3) the asthenospheric mantle beneath the plate boundary and (4) the asthenospheric mantle beneath the North America Plate for a model with a random initial olivine CPO are displayed in Fig. 5. Both the orientation of the olivine CPO and its intensity, defined by the J index (Bunge 1982), vary strongly between the four domains (Fig. 5, profiles A–C).

In the lithospheric mantle, the strongest olivine CPO is observed beneath the plate boundary where finite strain reaches $\gamma = 4$ (i.e. the lateral displacement is four times the width of the shear zone at the plate boundary). In this domain: [100] axes are strongly aligned along the Y direction, that is, parallel to the orientation of the plate

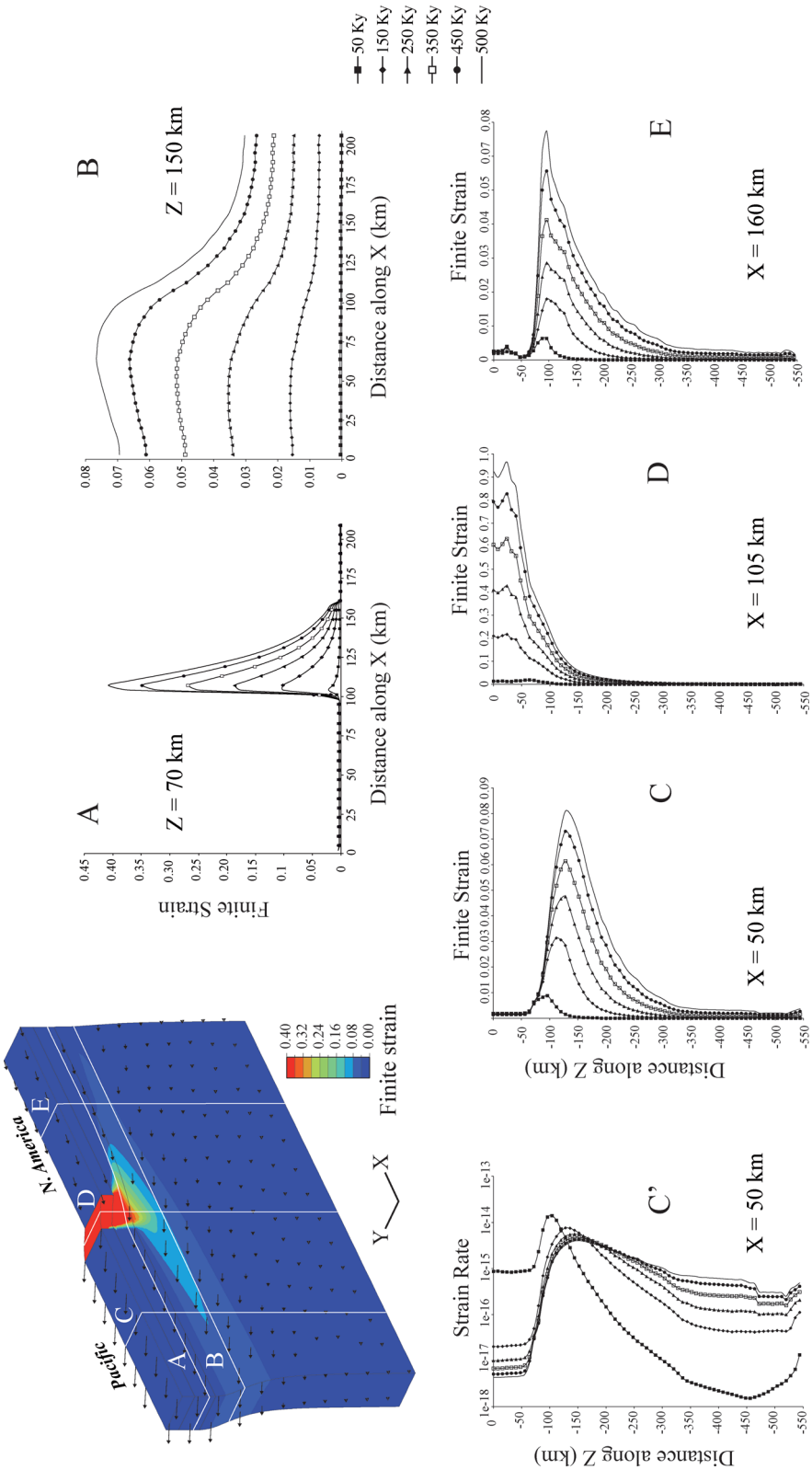

Figure 3. Top left: Finite strain (second invariant) and velocity fields after 0.5 Myr of deformation in the model 'TDT60', where a hot geotherm is imposed on the North America Plate within 60 km of the plate boundary. White lines represent the profiles. Top right: Temporal evolution of the second invariant of the finite strain in horizontal sections at (A) 70 km and (B) 150 km depth. Note the factor 10 difference in the scales between the finite strain axes on the different axes. Bottom: Temporal evolution of the second invariant of the finite strain in vertical sections at (C) $X = 50$ km, (D) $X = 105$ km and (E) $X = 160$ km (right). C' represents the temporal evolution of the strain rate in neutral section (C).

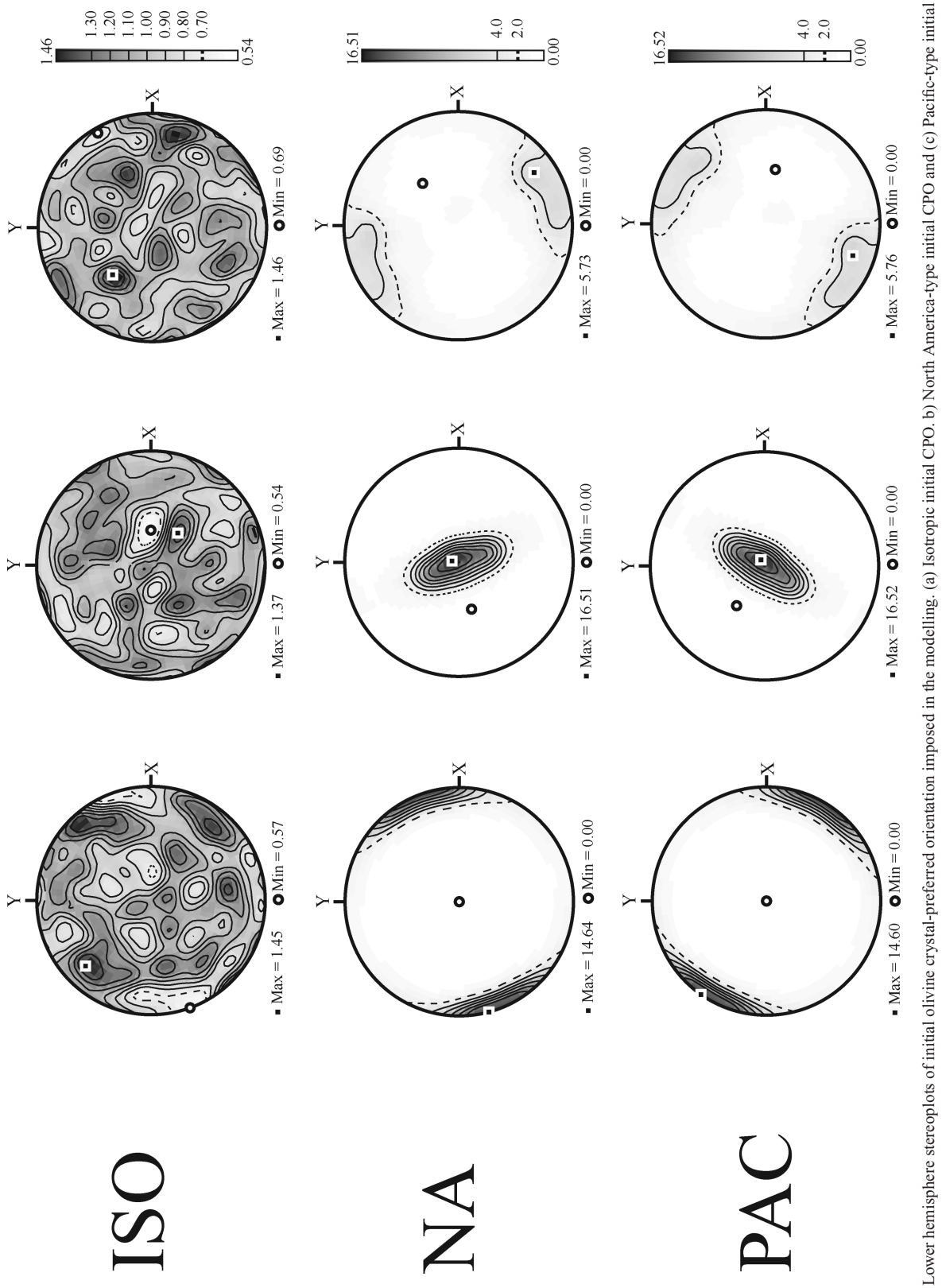

Figure 4. Lower hemisphere stereoplots of initial olivine crystal-preferred orientation imposed in the modelling. (a) Isotropic initial CPO. b) North America-type initial CPO and (c) Pacific-type initial CPO.

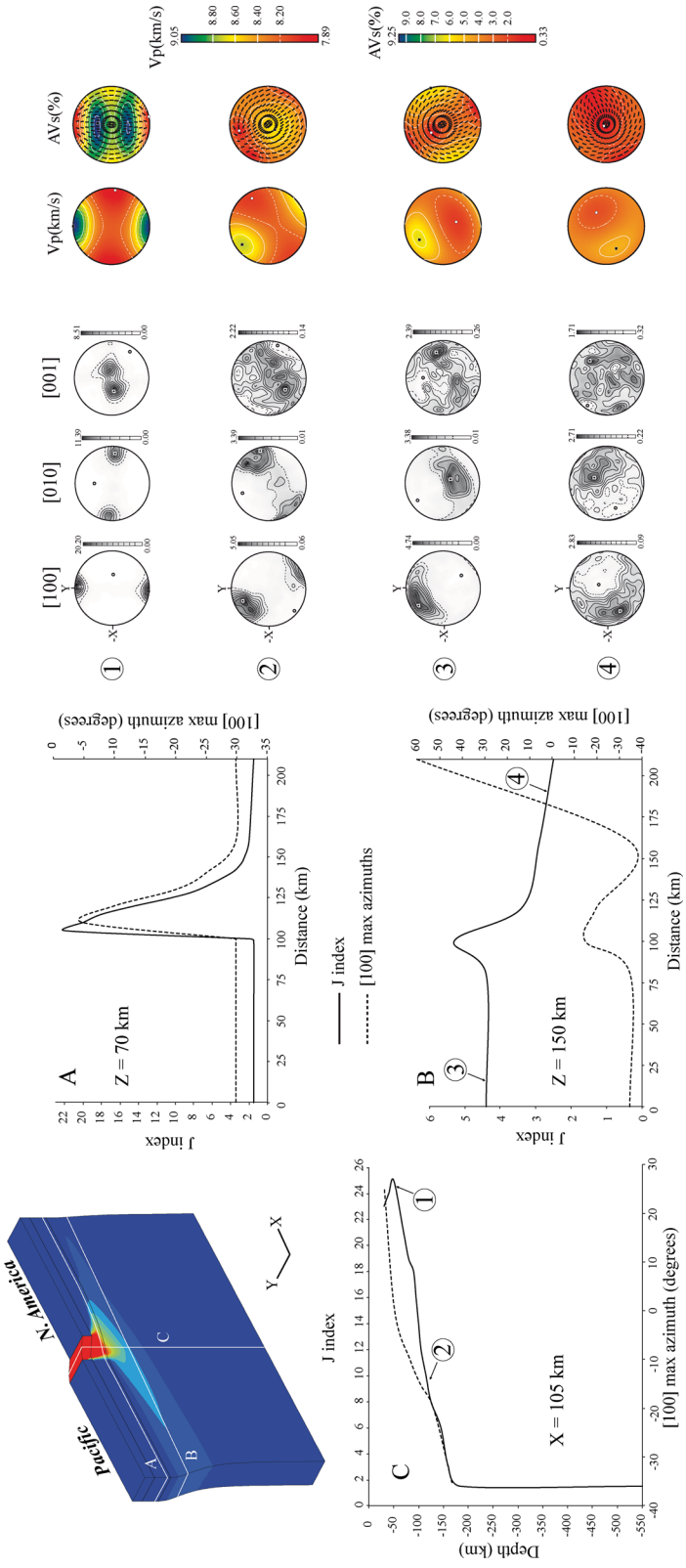

Figure 5. Left-hand side: Evolution of the strength of the olivine CPO, defined by the *J* index, which is the volume-averaged integral of the squared orientation densities (Bunge 1982), and of the orientation of the maximum concentration of olivine [100] along cross-sections in the model 'TDT60', where a hot geotherm is imposed on the North America Plate within 60 km of the plate boundary. Note that [100] axes oriented at 0° are parallel to the strike of the fault. Location of the cross-sections presented on a 3-D view of the finite strain at the end of the experiment. (A) Horizontal cross-section at 70 km depth, (B) horizontal cross-section at 150 km depth and (C) vertical cross-section beneath the plate boundary (at $X = 105$ km). Right-hand side: olivine crystal-preferred orientations and seismic properties (calculated for 70 per cent olivine–30 per cent enstatite aggregates) in representative domains of the model. Localization of the domain indicated on the diagrams on the left-hand side. All data are presented in lower hemisphere stereoplots in the thermomechanical model reference frame: $+X$ to the right, $+Y$ to the top and $+Z$ vertical upwards.

boundary (Fig. 5, fabric 1); [010] axes are oriented parallel to the *X* direction, that is, in the horizontal plane and perpendicular to the plate boundary orientation; and [001] axes are mostly vertical. This olivine CPO is consistent with a plate boundary deforming preferentially by strike-slip (Tommasi *et al.* 1999). This fabric results in strong anisotropy both for compressional and shear waves (Fig. 5, fabric 1, right panel). The maximum anisotropy (∼9.25 per cent) is observed for shear waves propagating at 45° from the vertical. This value decreases to approximately 8 per cent for vertically propagating teleseismic waves [such as *S*(*K*)*KS* waves]. The polarization of the fast quasi-shear wave is parallel to the plate boundary trend, as expected above a strike-slip structure (Tommasi *et al.* 1999).

The evolution of the CPO strength along a horizontal profile at 70 km depth (Fig. 5, profile A) closely follows the finite strain evolution (Fig. 3, profile A); almost random olivine CPO (*J* index <2) characterizes the entire Pacific lithosphere and the North America lithospheric mantle more than 60 km away from the plate boundary. In the hotter domain beneath North America, the olivine CPO intensity in the lithospheric mantle decreases linearly with the distance from the plate boundary. This variation in CPO strength is accompanied by a gradual anticlockwise rotation of the maximum concentration of olivine [100] axes from fault parallel to directions at ∼30° from the fault trace.

The sublithospheric mantle has more homogeneous olivine CPO intensities; *J* indices vary between 2 and 5.5 (Fig. 5, profile B). The strongest olivine CPO are still observed beneath the plate boundary ($\gamma = 1$), but clear olivine CPO also develop beneath both plates. As in the lithospheric mantle, the olivine CPO strength is correlated to the finite strain distribution (Fig. 3, profile B), but the maximum beneath the plate boundary is less pronounced. The CPO orientation varies however strongly between the three domains.

In the Pacific sublithospheric mantle (fabric 3), olivine [100] axes are predominantly oriented at *ca.* −45° from the fault trace (positive clockwise), ranging from subhorizontal to weakly dipping; [010] axes dip steeply; [001] axes are strongly dispersed. This olivine CPO is consistent with horizontal simple shear oriented at −45° relative to the fault plane and hence with an asthenospheric deformation in response to the displacement of the 'Pacific' Plate. The subhorizontal orientation of the olivine [100] axes and the moderate CPO (*J* index ∼4.5) due to the rather low finite strain ($\gamma = 0.8$) accumulated in 5 Myr results in lower anisotropy for both compressional and shear waves than beneath the plate boundary (Fig. 5, profile B and fabric 3). A high birefringence of 6 per cent would be recorded by horizontally propagating waves with *SH* waves faster than *SV* but vertically propagating teleseismic shear waves will sample intermediate birefringence (3 per cent) directions and longer paths than beneath the plate boundary will be necessary to produce detectable splitting delays (70-km-thick anisotropic layer will produce splitting delays of ∼0.5 s). *Vs1* polarization planes for vertically propagating waves will be parallel to the dominant orientation of the [100] axes of olivine, that is, at −45° from the fault trace.

The sublithospheric mantle beneath the plate boundary is characterized by olivine CPO and seismic properties intermediate between those in the lithospheric mantle beneath the boundary and those beneath the Pacific Plate (Fig. 5, fabric 2 and profile C). Both [100] and [010] olivine axes maxima are subhorizontal and the [001] axes maximum concentration, although much weaker, is subvertical. However, [100] axes are no longer oriented parallel to the plate boundary, but at around −30° from the fault trace. This olivine CPO is coherent with a vertical foliation and a subhorizontal lineation, that is, with a strike-slip kinematics (Tommasi *et al.* 1999). The lineation and hence the maximum concentration of [100] axes rotate however anticlockwise towards a direction at −30° to the strike of the fault and olivine [010] axes are dispersed in a girdle along a subvertical plane, suggesting an increasing contribution with depth of deformation associated to the drag of the asthenosphere by the displacement of the Pacific plate. This suggests coupling to the plate boundary kinematics even at sublithospheric depths (∼125 km depths). Another possible explanation for the increase in obliquity of the lineation relatively to the plate boundary trend with depth is the lower finite strain due to the more distributed deformation (Savage *et al.* 2004). However the change in orientation of the [010] axes, whose subvertical population increases with depth, favours the first hypothesis. Although the olivine CPO strength beneath the plate boundary decreases with depth (Fig. 5, profile C), the rotation of the CPO, in particular the change in the [010] axes orientation, maintains relatively high amounts of anisotropy for vertically propagating teleseismic shear waves (>5 per cent) up to 150 km depth (Fig. 6). Strong anisotropy over 150 km depth will result in large splitting delays for stations localized close to the plate boundary, but the variation with depth of the polarization directions of the fast shear waves from fault parallel direction to oblique (−45°) to the fault trace will induce complexities in the measured anisotropic signal. The polarization anisotropy for horizontally propagating shear waves increases with depth; *SH* waves are faster than *SV* but the birefringence depends on the propagation direction.

The sublithospheric mantle beneath the North America Plate (Fig. 5, fabric 4 and profile B) is characterized by weak CPO (*J* index ∼2.5), consistent with the lower plate velocity and finite strains ($\gamma = 0.3$) in the asthenosphere (Fig. 3, profile E). Olivine CPO is characterized by a girdle of [100] axes along a plane dipping of ∼20° towards the plate boundary, with a weak maxima subparallel to the plate displacement direction, that is, at −120° from the strike of the fault; [010] axes form a weak maximum normal to the [100] girdle and [001] are very dispersed. As the CPO, seismic anisotropy is very weak (the maximum birefringence, observed for horizontally propagating shear waves, is 3 per cent with *SH* waves faster than *SV*). The minimal birefringence is reached for vertically propagating waves. This region is thus quasi-isotropic for *SKS*-type waves.

To summarize, these models are characterized by three domains with different seismological responses. The Pacific Plate will have a rather simple signal with polarization of fast *SKS* waves parallel to the APM. Close to the plate boundary, the seismic anisotropy signal will be more complex, due to the anticlockwise rotation of olivine CPO at depth, from fault parallel to –30° to –45° from the fault trace directions. Finally, the sublithospheric mantle beneath the North America Plate will be isotropic for *SKS* waves.

3.2.2 'North America' initial olivine CPO

Olivine CPO and seismic properties at 70 and 125 km depth beneath the plate boundary and in the sublithospheric mantle (150 km depth) beneath both plates in a model in which the initial olivine CPO correspond to the one expected to develop in response to the displacement of North America Plate relatively to a fixed deep mantle are presented in Fig. 7.

The lithospheric mantle beneath the plate boundary is characterized by olivine [100] axes strongly oriented along the plate boundary strike (Fig. 7A), and [010] axes are mainly subvertical; [001] axes are predominantly oriented normal to the fault (*X* direction) and subhorizontal. Thus, despite the strike-slip deformation regime imposed at the plate boundary, the olivine CPO is not

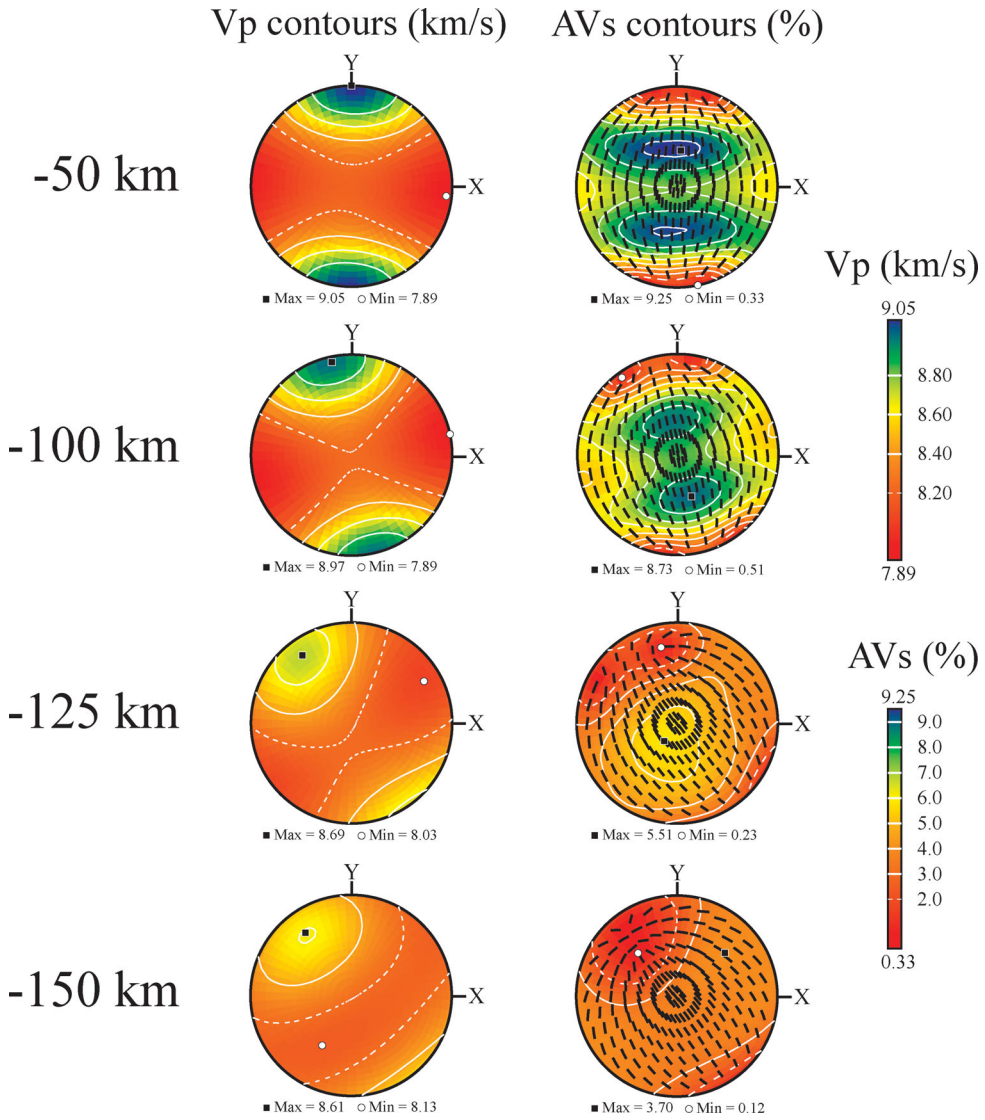

Figure 6. Lower hemisphere stereoplots in the thermomechanical reference frame ($+X$ to the right, $+Y$ to the top and $+Z$ vertical upwards) presenting the seismic properties (calculated for 70 per cent olivine–30 per cent enstatite aggregates) of domains localized at different depths (50, 100, 125 and 150 km from top to bottom) beneath the fault zone.

consistent with a vertical foliation. The horizontal foliation characteristics from the initial CPO are preserved; the strike-slip deformation beneath the plate boundary essentially reorients the [100] axes towards a fault parallel direction. The [010] axes maximum density decreases however (from 16 in Figs 4–9 in Fig. 7A), indicating some reorientation of this axis towards the horizontal. This CPO results in strong anisotropy for both compressional and shear waves. The maximum anisotropy is still observed for shear waves propagating at 45° from the vertical. This value decreases to approximately 6 per cent for vertically propagating teleseismic waves, which can still induce large delay times. The polarization of the fast quasi-shear wave is subparallel to the plate boundary orientation.

In the sublithospheric mantle beneath the plate boundary (Fig. 7C), at 125 km depth, olivine CPO is characterized by [100] axes predominantly oriented subhorizontal at *ca.* –45° from the fault trace and by subvertical [010] axes. This olivine CPO is consistent with the one predicted to develop by asthenospheric drag beneath a plate moving at –45° from the strike of the plate boundary. It is however much stronger than those obtained at the same depth in the model with an initially random olivine CPO (Fig. 5, fabric 2), since it evolves by reorientation of a strong pre-existing CPO (Fig. 4). Despite being strong, these olivine CPO result in weak-to-moderate anisotropy (4–6 per cent) for vertically propagating waves with fast quasi-shear waves polarized at –45° from the direction of the plate boundary. Strong polarization anisotropy (>7 per cent) with *SH* waves faster than *SV* will however be observed for horizontally propagating shear waves with backazimuths parallel to the plate boundary or at 45° from it.

In the Pacific sublithospheric mantle (Fig. 7B), olivine CPO hardly differs from the initial CPO. [100] axes are mainly oriented at *ca.* –120° from the fault trace, in the horizontal plane, [010] axes are vertical and [001] are close to fault parallel in the horizontal plane. Asthenospheric drag beneath the Pacific Plate results in a rotation by 10°–15° of the initial CPO, but finite strains are not large enough to fully reorient it along the Pacific APM. This CPO results in rather low polarization anisotropy (∼4 per cent) for vertically propagating shear waves and produces fast directions that are close to normal to the plate boundary. Strong polarization anisotropy (>8 per cent) with *SH* waves faster than *SV* will however be observed for horizontally propagating shear waves

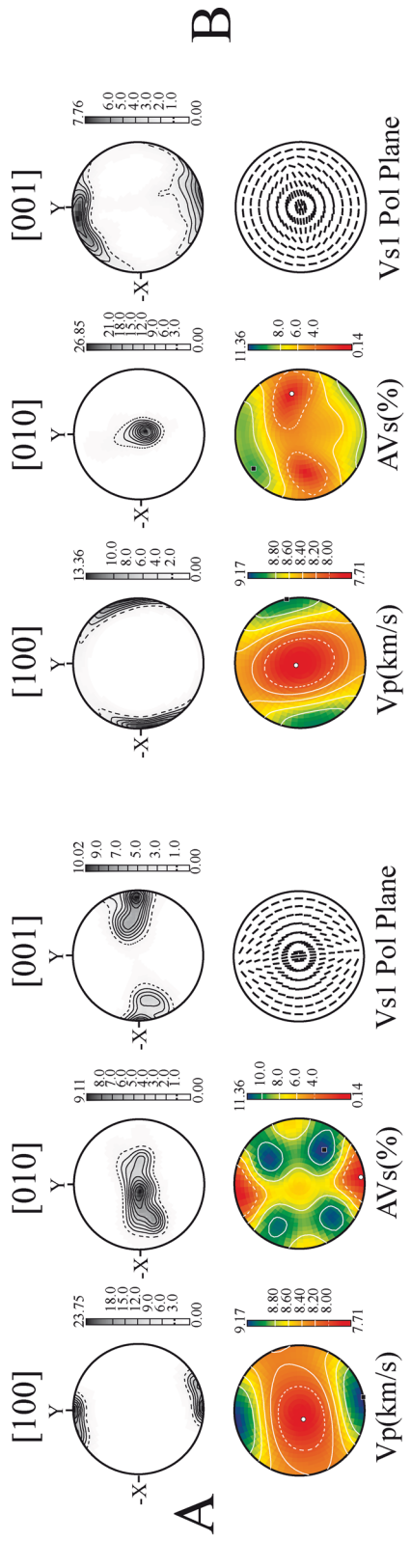

Figure 7. Olivine crystal-preferred orientations and seismic properties in representative domains for a model with an initial 'North America'-type olivine CPO. Data are presented in lower hemisphere stereoplots in the thermomechanical model reference frame: $+X$ to the right, $+Y$ to the top and $+Z$ vertical upwards. A, B, C and D domains, respectively, correspond to 1, 3, 2 and 4 domains in Fig. 5.

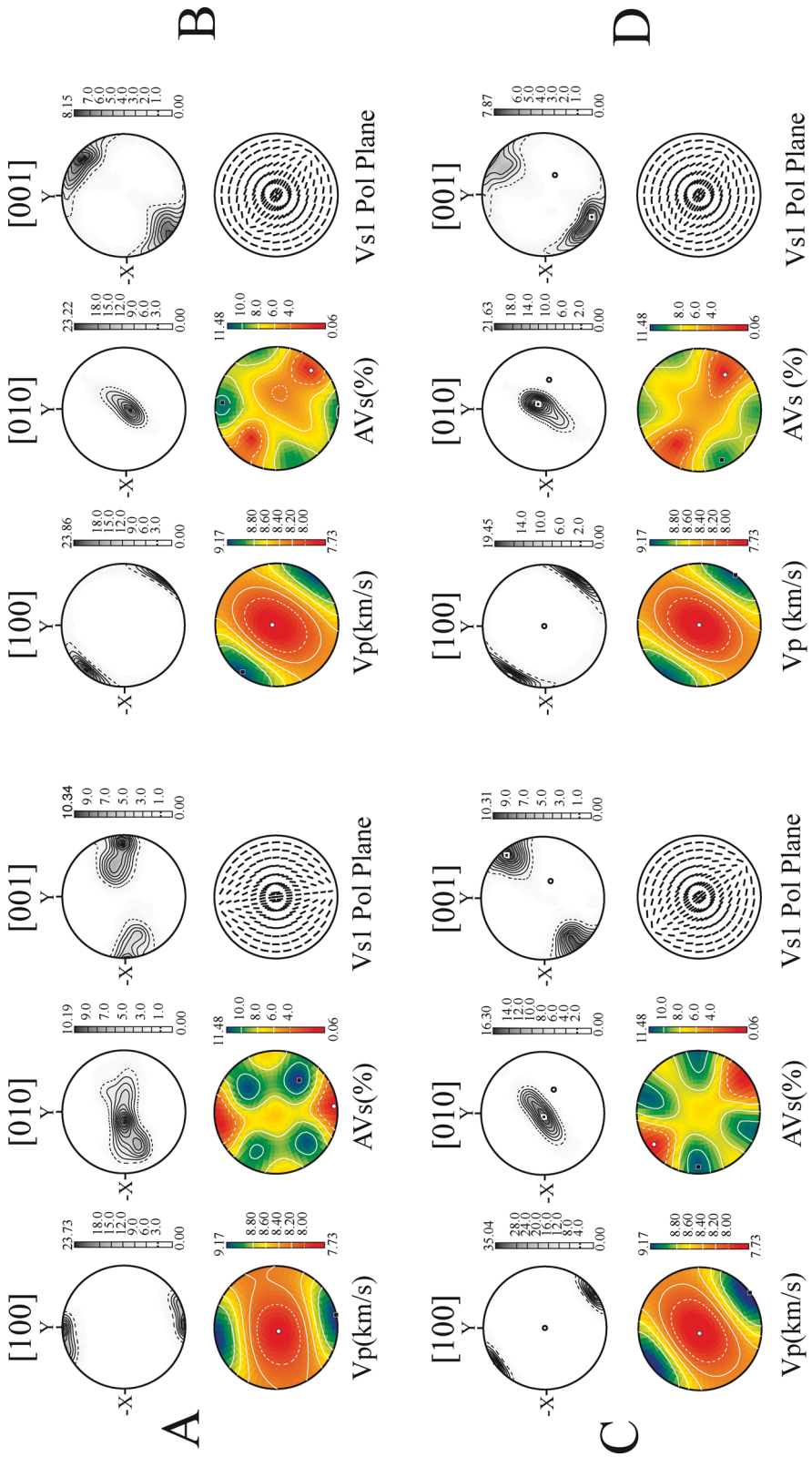

Figure 8. Olivine crystal-preferred orientations and seismic properties in the same representative domains as Fig. 7 for a model with an initial 'Pacific'-type olivine CPO. Data are presented in lower hemisphere stereoplots in the thermomechanical model reference frame: $+X$ to the right, $+Y$ to the top and $+Z$ vertical upwards.

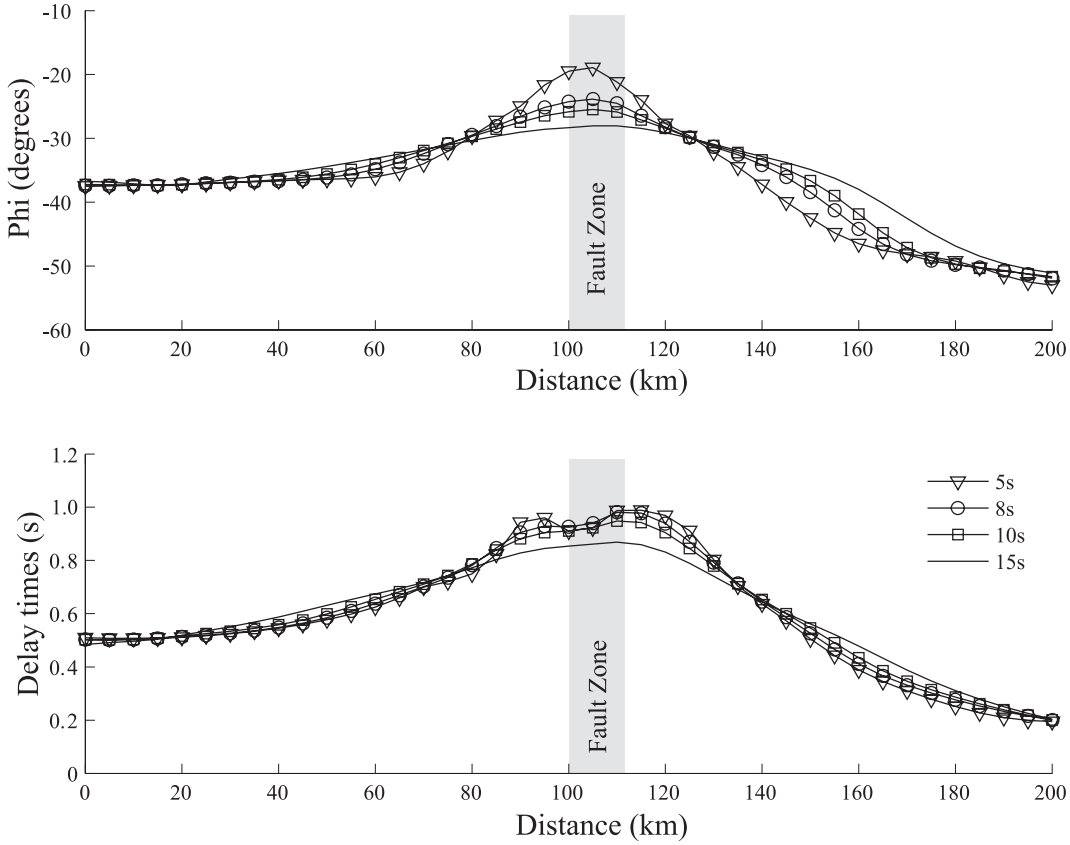

Figure 9. Fast-polarization directions according to the strike of the fault (top panel) and splitting delays (bottom panel) in a profile normal to the plate boundary obtained through a multichannel analysis of synthetic seismograms computed for the 'TDT60' model with initially random olivine CPO using the spectral element method for various dominant periods: 5 s (open triangles); 8 s (open circles); 10 s (open squares) and 15 s (solid line). Grey domains represent extent of the trace of the fault zone at surface of the model.

with backazimuths from parallel to 45° from the fault plane. Finally, olivine CPO and seismic properties in the sublithospheric mantle at 150 km depth beneath North America Plate (Fig. 7D) obviously present an olivine CPO very close to the initial one. As beneath the Pacific Plate, shear wave anisotropy for vertically propagating waves is relatively weak beneath North America (around 4 per cent).

3.2.3 'Pacific' initial olivine CPO

Olivine CPO and seismic properties at 70 and 125 km depth beneath the plate boundary and in the sublithospheric mantle (150 km depth) beneath both plates in a model in which the initial olivine CPO corresponds to the one expected to develop in response to the displacement of Pacific Plate relatively to a fixed deep mantle are presented in Fig. 8. In all domains, olivine CPO hardly differs from the initial one. The most significant variations are observed in the lithospheric mantle beneath the plate boundary (Fig. 8A), where the olivine [100] axes are reoriented towards a fault parallel direction. [010] axes are dispersed along vertical plane normal to the fault, but still preserve a subvertical maximum. Strain rates beneath the plate boundary are thus sufficiently high to reorient the [100] axes parallel to the plate boundary strike in 5 Myr but not to induce a complete reorientation of the olivine [010] axes. This reorientation is less developed at deeper levels beneath the plate boundary, because of the lower strain rates associated with a more distributed deformation. For instance, at 150 km depth beneath the plate boundary (Fig. 8B), [100] axes are predominantly oriented at –45° from the strike of the fault. As expected, olivine CPO do not change significantly in the sublithospheric mantle beneath the Pacific Plate (Fig. 8C). Variations are also minor in the sublithospheric mantle beneath the North America Plate (Fig. 8D), because of the low strain rates and hence strains in this region.

Seismic properties are, by consequence, rather homogeneous across this model. Anisotropy for vertically propagating shear waves is moderate (∼6–7 per cent). The polarization of fast quasi-shear waves is at –30° to –45° from the fault plane in most of the model, except in the lithospheric mantle beneath the plate boundary, where it is close to fault parallel. The birefringence of horizontally propagating shear waves depends strongly on the backazimuth but *SH* waves are always faster than *SV*. Compressional wave anisotropy is strong, with horizontally propagating waves faster than vertically propagating ones over the entire model.

3.3 *SKS* splitting analysis on synthetic seismograms

We have produced synthetic seismograms for the three models (different initial olivine CPO) presented earlier. These synthetic seismograms were analysed with both the Silver & Chan (1991) and the multichannel (Chevrot 2000) methods.

3.3.1 Initially random olivine CPO

Splitting parameters obtained from a multichannel analysis of synthetic data for stations located every 5 km along the *X* direction assuming a complete backazimuthal coverage are presented in Fig. 9.

This method gives, at each station, the delay time and the direction of polarization of the fast shear wave averaged over the Fresnel volume; it tends therefore to smooth the lateral variations of the seismic anisotropy in the model. Since the size of the Fresnel zone depends on the dominant period of the wave, we performed the computation at four different dominant periods: 5 s (open triangles), 8 s (open circles), 10 s (open squares) and 15 s (solid line), corresponding to wavelengths of approximately 25, 40, 50 and 75 km, respectively.

The dominant period has a strong influence on the measured direction of polarization of the fast quasi-shear wave (Fig. 9). For a dominant period of 5 s, sharp lateral variations of ϕ are observed. Three different domains may then be defined. In the Pacific Plate more than 30 km away from the plate boundary, fast-polarization directions are homogeneous at *ca.* –40° from the fault trace (positive clockwise) from the trace of the fault to the left. These directions are subparallel to the APM direction of the Pacific Plate and in good agreement with CPO in the sublithospheric mantle beneath the Pacific Plate. Within 30 km from the plate boundary, on both plates, directions of polarization vary rapidly, reaching a direction close to –20° from the fault plane above the plate boundary. This rotation reflects the influence of the strike-slip deformation in the plate boundary on seismic anisotropy. Further right to the fault, directions of polarization rotate anticlockwise, reaching –60° relative to the fault plane in the right limit of the model. This domain is also characterized by low delay times (<0.5 s), consistently with the low strains and weak CPO in the sublithospheric mantle beneath the North America Plate. Waves with a dominant period of 15 s show a different pattern. Their wavelength is larger than the width of the high strain domain at the plate boundary. The fast-polarization directions do not change as a function of the distance to the plate boundary; they vary by less than 10° across the entire model with continuous gradients.

Measuring splitting at different periods allows us to probe seismic anisotropy at different scales thus improving spatial resolution (Favier & Chevrot 2003; Chevrot 2006; Hammond *et al.* 2010). Fig. 9 shows that the fast-polarization directions for the four periods crosscut at 20 km left and 30 km to the right of the plate boundary, recording the presence at depth of a lateral change in anisotropic properties. One may interpret the domain delimited by the two inflexions in the fast-polarization curves as the maximum lateral extent of the strike-slip related deformation. In contrast, splitting delays are similar for all periods (Fig. 9). The four curves show a linear increase of the delay time from 0.5 s in the Pacific Plate far from the boundary to approximately 1 s (slightly less for longer periods) at the plate boundary followed by a decrease to close to null values in the North America Plate far from the plate boundary. In conclusion, apparent splitting parameters obtained from a multichannel analysis of full-wave synthetic seismograms are consistent with the modelled CPO (Fig. 5), but show smoother lateral variations due to averaging anisotropic properties over Fresnel zones.

Splitting parameters obtained using the same full-wave synthetics, but analysed with the single-event Silver & Chan (1991) method (S&C hereafter) are presented in Fig. 10. With this method, averaging of individual splitting parameters measured for each seismogram is necessary for comparison with the multichannel method. We thus stack the error maps of single-event measurements for each station, as proposed by Wolfe & Silver (1998). To first order, results from the two analysis methods are similar but the multichannel analysis produces a smoother signal, especially in the weakly anisotropic domains. The variations of the fast-polarization directions in the

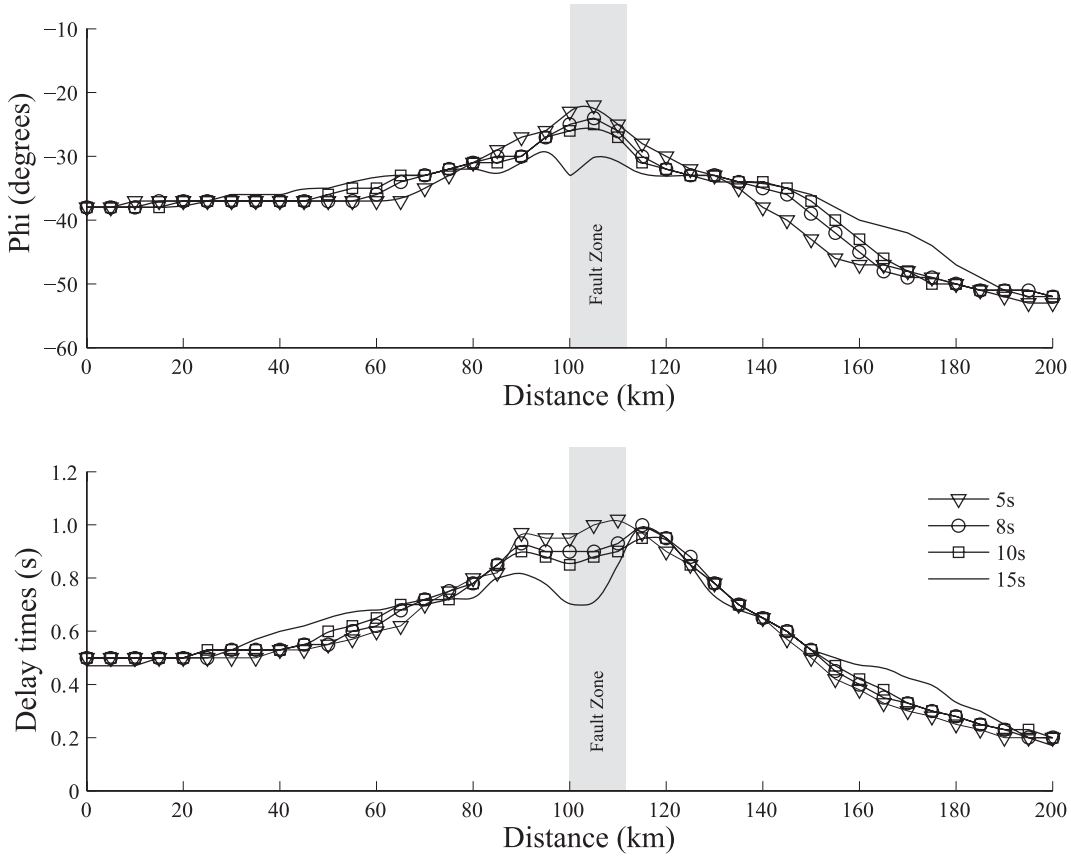

Figure 10. Same as Fig. 9 but splitting measurements were performed using the Silver and Chan method and stacked using the Wolfe and Silver approach.

vicinity of the plate boundary for a dominant period of 15 s are even less clear, indicating a lower sensitivity of the S&C approach to smooth variations of the anisotropic properties compared to the multichannel method. This lower sensitivity is also evidenced by the delay times that show strong dispersion in the vicinity of the fault zone for 15 s of dominant period.

Splitting measurements were also performed on synthetic seismograms computed with ray theory using both the multichannel SI approach and the S&C method (Figs 11 and 12). In this case, the waves sample seismic anisotropy along a vertical ray path. Being a single-event method, the S&C method allows studying the variations of the splitting parameters as a function of the initial polarization of the incoming waves. A 90° periodicity in the variation of splitting parameters indicates a vertical change in anisotropic properties, which are commonly modelled as two (or more) distinct anisotropic layers (Savage & Silver 1993; Silver & Savage 1994). Application of this method to our models will therefore allow us to test whether it can also detect gradational changes in anisotropy.

Splitting parameters obtained on ray theory synthetics analysed with the S&C method [stacked using Wolfe & Silver (1998) approach] and with the multichannel method are displayed in Fig. 11. The two methods of splitting analysis give similar trends, except in the North America Plate far from the plate boundary. In this region the multichannel method is superior, clearly detecting the weak anisotropy in this domain. Fast-polarization directions and delay times are quite homogeneous at –30° relative to the fault plane beneath the Pacific Plate. Fast-polarization directions rotate rapidly to fault parallel directions and delay times increase beneath the plate boundary (between 100 and 110 km). Then fast polarization directions reorient back to –40° and delay times decrease in a continuous manner within 60 km from the plate boundary. More than 60 km away from the boundary, fast polarization directions rotate anticlockwise towards –60° relative to the plane, but the associated delay times are very low or null.

As expected, since they correspond to a high-frequency approximation, synthetics produced with ray theory result in sharper lateral variations of splitting parameters (Fig. 11) than those obtained on full-wave synthetics (Figs 9 and 10). The apparent width of the shear zone derived from the analysis of ray theory synthetics is 30–40 km to the right of the plate boundary. This width is nevertheless in good agreement with the 40 km width defined from the analysis of full-wave synthetic seismograms at different dominant periods (Fig. 9). Consistency is also observed between delay times measured on both ray theory and full-wave synthetics. The larger splitting delays of *ca.* 1 s are located between 90 and 130 km in all cases.

However, none of these approaches recovers the vertical complexity of structures beneath the plate boundary. Fig. 12 presents individual splitting measurements performed using the S&C method as a function of the initial polarization of the incoming wave for stations located at and far from the plate boundary. At station #10, located on the Pacific Plate far from the plate boundary (X = 50 km), fast-polarization directions and delay times are largely unaffected by changes in initial polarization (Fig. 12a). This is consistent with a single layer of anisotropy with a direction of polarization of the fast quasi-shear wave of *ca.* –35° relative to the fault plane. This fast-polarization direction and the measured delay time of 0.5 s are coherent with the olivine CPO in the sublithospheric mantle beneath the Pacific Plate in the model (Fig. 5, fabric 3 and profile B). The variations in fast-polarization direction around initial polarizations of 50° and 140°, mark the fast and slow directions of the medium; shear waves propagating along these directions see the medium as isotropic, causing artefacts with the S&C method.

Very different results are obtained at station #21 (X = 105 km), located at the plate boundary (Fig. 12b). The splitting parameters depend strongly on the initial polarization and show a 90° periodicity. Sharp variations of both fast-polarization direction and delay time occur around 80° and 170°. This pattern suggests a variation of anisotropy with depth (Silver & Savage 1994). This evidence for a vertically varying anisotropic structure beneath the plate boundary is consistent with the changes in orientation of the olivine CPO and seismic properties as a function of depth beneath the plate boundary (Figs 5 and 6). The apparent splitting values may indeed be fitted by a model composed by two anisotropic layers as described in Bonnin *et al.* (2010) but the apparent anisotropy parameters of the model that best fits the data (shown as a dotted line in Fig. 12b): $\phi_{up} = 38°$; $\delta t_{up} = 0.4$ s; $\phi_{low} = -14°$ and $\delta t_{low} = 1.4$ s (directions are according to the fault plane), are inconsistent with the vertical variation of the olivine CPO and seismic anisotropy of the input model (Figs 5 and 6). Similar 90° periodicity pattern is observed when analysing full-wave synthetics using S&C methods, with however differences in the shape of the variation induced by the wider volume sampled by these waves compared to the ray theory synthetics. As for ray theory synthetics, best-fitting two-layer models are inconsistent with the petrophysical inputs. These inconsistencies imply that the analysis of the variation of splitting parameters as a function of incoming wave backazimuth using simple two-layer models cannot be used to unravel smoothly varying splitting parameters such as those in our model.

Finally, at station #35 located in the North America Plate far from the boundary, delay times are either very low or very high and fast polarization directions cover all the possible range of directions (Fig. 12c). This pattern is typical of 'null' splitting measurements. It is therefore consistent with the input model. However, an unambiguous determination of an apparently isotropic region using individual measurements requires an excellent azimuthal sampling, which is rarely available with real data.

3.3.2 'North America' initial CPO

Averaged splitting parameters determined with the Wolfe & Silver (1998) method on synthetic seismograms computed by ray theory in a model in which the initial crystallographic fabrics are oriented by the differential motion between the North America Plate and a static deep mantle are displayed in Fig. 13. The major difference relative to the model with an initially random olivine CPO (Fig. 11) is the stronger anisotropy in the two plates far from the fault zone. Large delay times (around 3 s) are observed almost everywhere in the model due to the strong olivine CPO (Fig. 7) from the surface down to 300 km depth. The location of the plate boundary is only marked by variations of the fast-polarization directions.

Constant –120° from the fault plane fast polarization directions characterize both plates far from the boundary (Fig. 13), indicating that deformation associated with asthenospheric drag by the motion of the Pacific Plate is not strong enough to reorient the initial crystallographic fabric. Strong variations of fast-polarization directions are however observed within 50 or 75 km from the plate boundary on the Pacific and North America plates, respectively. These observations suggest that the maximum lateral extent of the influence of the plate boundary deformation reaches ∼125 km. This 125-km-wide zone represents a domain in the model where finite shear strains are over 50 per cent. Fast polarization directions vary from fault normal to –45° relative to the plate boundary and back to close to fault normal. They show no direct relation to the olivine CPO in the input model, in particular at the plate boundary. Averaged fast-polarization

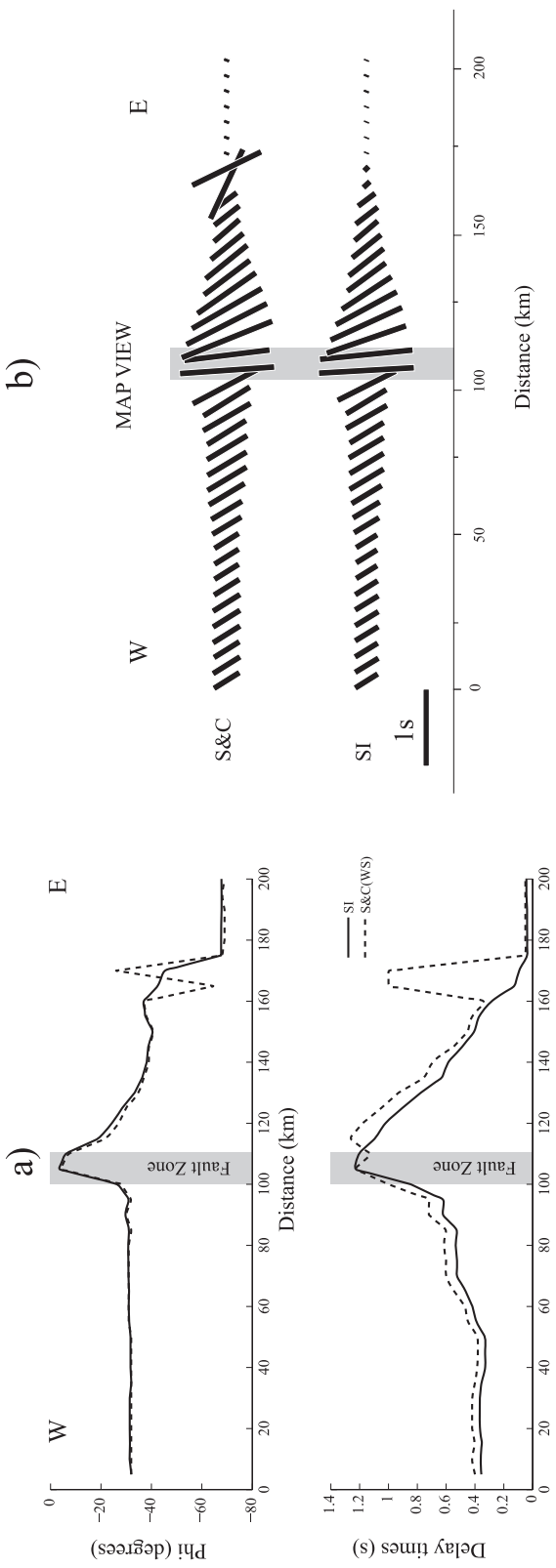

Figure 11. (a) Fast-polarization directions according to the strike of the fault and splitting delays in a profile normal to the plate boundary obtained using multichannel (SI, solid curve) and S&C (doted curve) methods on synthetics computed with ray theory for the 'TDT60' model with initially random olivine CPO. (b) Averaged splitting parameters represented in a map view. Direction and length of bars represent fast-polarization directions and splitting delays, respectively. Grey domains represent extent of the trace of the fault zone at the surface of the model.

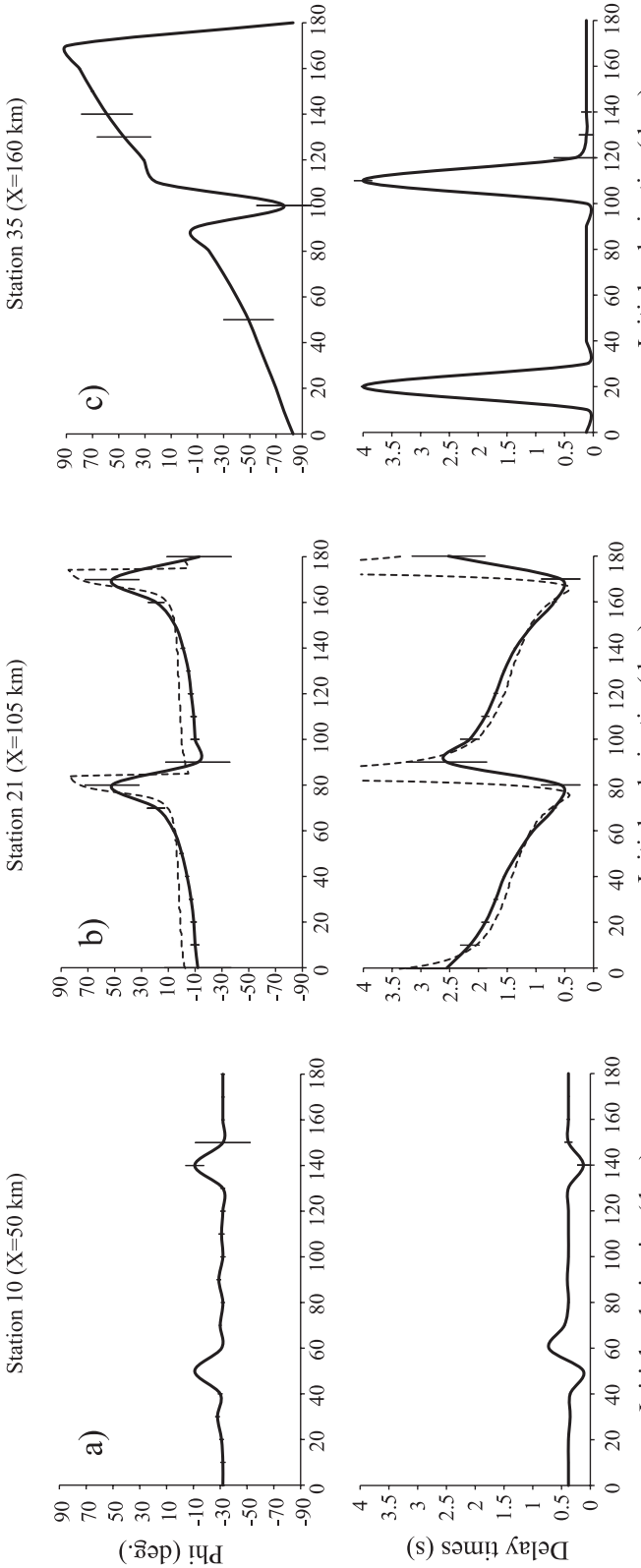

Figure 12. Individual splitting parameters as a function of the initial polarization of the synthetic wave for (a) station 10 at 50 km on the Pacific Plate; (b) station 21 at 105 km, that is, above the plate boundary and (c) station 35 at 160 km on the North America Plate in the 'TDT60' model with an initially random olivine CPO. Dotted curve at station 21 represents apparent splitting parameters derived from the best-fitting two-layer model discussed in the text: $\phi_{\rm up} = 38^\circ$, $\delta t_{\rm up} = 0.4$ s; $\phi_{\rm low} = -14^\circ$, $\delta t_{\rm low} = 1.4$ s.

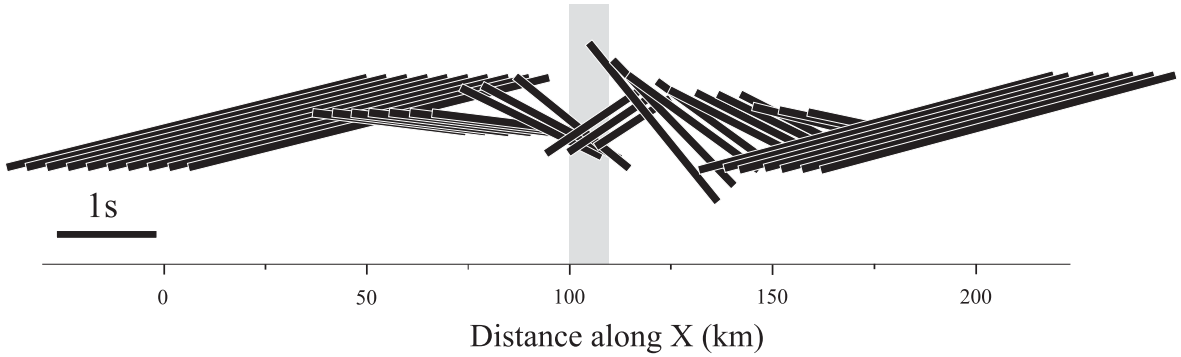

Figure 13. Averaged splitting measurements in map view for a 'TDT60' model in which the initial olivine CPO corresponds to the one formed in response to the absolute motion of the North America Plate. Measurements were performed using S&C method for synthetics computed under the assumption of the ray theory. Direction and length of bars represent fast-polarization directions and splitting delays, respectively. Zone in grey represent the fault zone domain.

directions in this part of the model are thus likely affected by the smooth variation of the anisotropy both laterally and vertically and we are not able to recover the input structure.

3.3.3 'Pacific' initial CPO

Averaged splitting parameters determined with the S&C method on synthetic seismograms calculated with ray theory in a model in which the initial crystallographic fabrics are oriented by deformation due to the velocity gradient between the Pacific Plate and a static deep mantle, and stacked with the Wolfe & Silver (1998) approach are presented in Fig. 14. Once again, delay times are extremely high (around 3 s), because the upper 300 km of the model display a strong initial olivine CPO (Fig. 8). Fast quasi-shear waves polarized at *ca.* –45° relative to the fault plane, consistent with the orientation of the olivine [100] axes in the initial CPO, are observed everywhere, except at the plate boundary where fast polarization directions are rotated into a more fault parallel orientation. Fast-polarization directions in the right part and central domain of the model are similar to those obtained with an initially random isotropic model (Fig. 11). They are however very different from those obtained in the model with an initial 'North America' olivine CPO (Fig. 13). This suggests that finite strains associated with the modelled plate boundary configuration are high enough beneath both the plate boundary and the faster moving Pacific Plate to produce a distinctive anisotropy signal in 5 Myr when the pre-existing olivine CPO is isotropic or coherent with the imposed deformation, but not when it is at a high angle from it. 5 Myr of constant deformation according to the modelled plate boundary configuration cannot therefore reorient the mantle fabric beneath North America from a Pacific-like to a North America-like trend. The hypothesis of progressive rotation of the fast-polarization directions in the Great Valley region (see Fig. 15 for localization) as a consequence of the westward displacement of the plate boundary, leading to reworking of Pacific-type crystallographic fabrics in the sublithospheric mantle through drag by North America APM (Bonnin *et al.* 2010) should likely be discarded in the light of these results.

4 DISCUSSION

4.1 Migration of the plate boundary and reorientation of crystallographic fabrics in the sublithospheric mantle

In this section, we focus on the asthenospheric deformation induced by the motion of the plate relative to the deep mantle (APM) and on the effect of the plate boundary migration in the APM reference frame. This deformation is particularly relevant for the San Andreas transform system, as it is one of the hypotheses for explaining the large-scale anisotropy patterns observed beneath California (Bonnin *et al.* 2010).

In the initially random models, asthenospheric deformation related to drag by the moving plates is clearly identified far from the plate boundary. It results in an orientation of the [100] crystallographic axes of the olivine oblique to the plate boundary beneath both the Pacific and North America plates and in vertical [010] axes (Fig. 5, fabrics 3 and 4, respectively). In the 5 Myr time span considered in this study, the olivine CPO produced by this

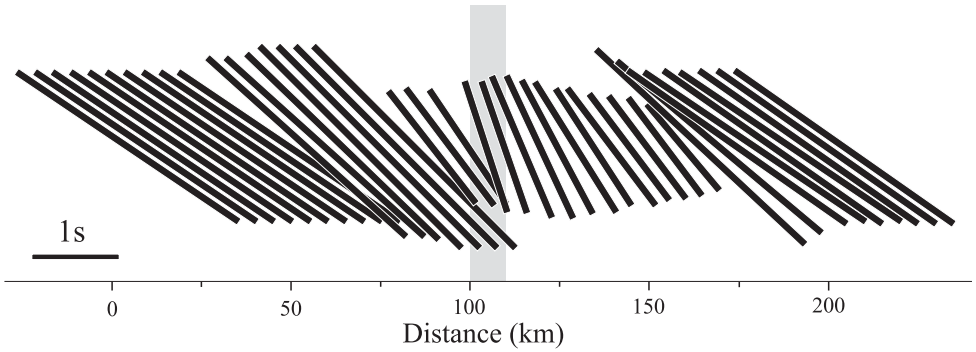

Figure 14. Averaged splitting measurements in map view for a 'TDT60' model in which the initial olivine CPO corresponds to the one formed in response to the absolute motion of the Pacific Plate. Measurements were performed using S&C method for synthetics computed under the assumption of the ray theory. Direction and length of bars represent fast-polarization directions and splitting delays, respectively. Zone in grey represent the fault zone domain.

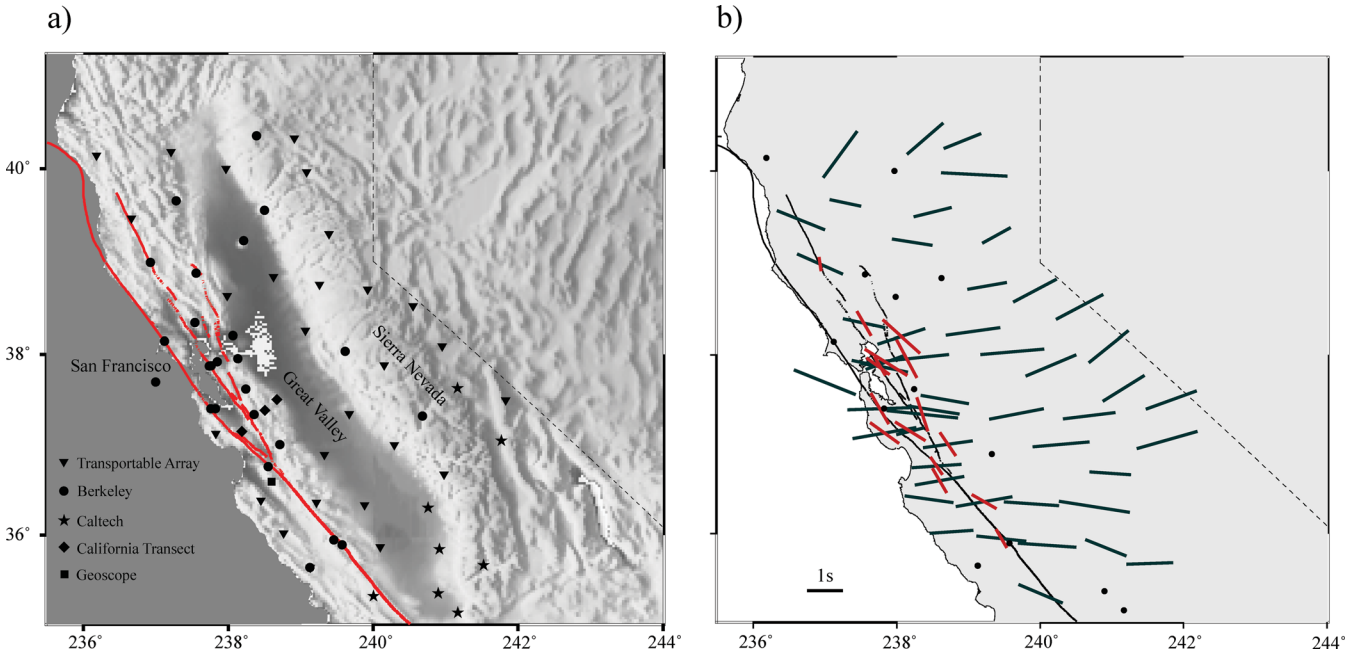

Figure 15. (a) Map of the Northern California region presenting the network used in Bonnin *et al.* (2010), the different zones named in the text and the main faults (red lines). (b) Map presenting averaged splitting parameters (single dark green bars) and two-layer models (red (upper layer) and dark green (lower layer) bars) from Bonnin *et al.* (2010); directions of the bars indicate the direction of polarization of the fast waves; length of the bars are proportional to the delay times.

deformation beneath the Pacific Plate are relatively weak (*J* index ∼5, Fig. 5B), resulting in relatively low shear wave anisotropy (∼4 per cent for vertically propagating shear waves). The weak anisotropy is partially balanced by the relative large thickness of the anisotropic layer (100–150 km, Fig. 3B). As a consequence, stations on the Pacific Plate display delay times of 0.5 s. These values are low compared to the 1.5 s measured by Bonnin *et al.* (2010). The Pacific lithosphere in central California region is however several tens of million years old, whereas olivine CPO in the models were calculated for only 5 Myr of deformation.

Similarly, olivine CPO produced by the velocity gradient between the North America Plate and the deep mantle are very weak and result in a medium that is close to isotropic for vertically propagating waves (Fig. 5, fabric 4). Considering the North America APM, very long time spans would be necessary to produce the 1.5 s of splitting delay observed in central California east of the plate boundary. Yet these calculations consider an initially random olivine CPO, while mantle rocks are long-lived and hence never isotropic. On the other hand, the possible development of an asthenospheric window 5–9 Ma (Atwater 1970; Dickinson & Snyder 1979; Dickinson 1997) rules out the preservation of olivine CPO controlled by the North America Plate motion for very long time spans in this region. An APM-related origin of the anisotropy suggested beneath central California should thus be discarded. Active asthenospheric processes in relation with the opening of the asthenospheric window as proposed by Ozalaybey & Savage (1995) or with the sinking of the remnants of the Farallon slab as preferred by Hartog & Schwartz (2000) are thus more plausible explanations for the observed splitting pattern. Anisotropy beneath central California may also result from the velocity gradient between an active asthenospheric flow and the APM of the North America and Pacific lithospheres as proposed by Silver & Holt (2002).

Bonnin *et al.* (2010) proposed that the smooth rotation of the directions of fast polarization in the Great Valley (Fig. 15) could record a progressive reorientation of olivine CPO in the sublithospheric mantle. In this model, westward migration of the plate boundary would result in reorientation of olivine CPO formed in response to the motion of the Pacific Plate towards a new orientation coherent with the shearing induced by westward motion of the North America Plate. The present models show however that the motion of the North America Plate is too slow to effectively reorient a pre-existing fabric in 5 Myr. The models with different inherited crystallographic fabrics in the mantle confirm this observation, as the anisotropic signal in the easternmost part of the model always corresponds to the initial crystallographic fabric (Figs 7 and 8). In contrast, the deformation associated with the plate boundary fully reorients the initial crystallographic fabrics down to asthenospheric depths in the vicinity of the fault zone. Strong coupling between the lithosphere and the asthenosphere thus likely controls the reorientation of the sublithospheric mantle fabrics during progressive westward motion of the Pacific/North America Plate boundary.

4.2 Lateral extent of the plate boundary-related deformation

Analysis of the finite strain and strain rate distributions in the thermomechanical model 'TDT60' (Fig. 3) shows that, in the lithospheric mantle, the deformation associated with the strike-slip plate boundary is accommodated in an asymmetric shear zone with a sharp limit on the Pacific side. The highest strain rates occur at the limit between the two plates. Strain rates decrease then linearly (by a factor 10) within the 60-km-wide hotter domain of the North merica Plate. A sharp decrease in strain rate by two orders of magnitude occurs at the end of this domain. This variation in strain rates is closely recorded by the olivine CPO evolution in a cross-section at 70 km depth (Fig. 5A). At 150 km depth, the plate boundary zone is still characterized by an asymmetric strain rate distribution, but its limits are diffuse. Analysis of the olivine CPO at 150 km depth

(Fig. 5B) shows nevertheless a 50- to 60-km-wide asymmetric domain beneath the North America Plate characterized by a sharp reorientation of the maximum of [100] axes directions from –45° to the fault plane to more fault parallel directions followed by a gradual return towards –45° orientations. CPO at these depths becomes however weak (J index < 3) more than 25 km away from the boundary. The plate boundary extent in the mantle varies therefore with depth from 60 km to less than 50 km.

These observations are fully consistent with previous 2-D finite-element models of strike-slip plate boundaries by Savage *et al.* (2004). In their study, models with a 80-km-wide low-viscosity domain directly east the fault zone (models 'Oneside' and 'WUS + PAC') also showed asymmetric strain localization with high strain rates up to 60 km far from the fault and progressive decrease of the strain rates as a function of the distance to the fault trace. Relating seismic anisotropy to the directions of maximum extension or to the velocity field in the model, Savage *et al.* (2004) observed, in the low-viscosity domains, a progressive rotation of the fast splitting directions from close to parallel to the fault within 10 km of it to ∼30° from the trace of the fault at the edge of the viscosity anomaly. This rotation was associated with a decrease of the delay time. The pattern of splitting parameters variation in these models is thus very similar to the one predicted in our study using ray theory synthetics on model 'TDT60' (Fig. 11).

Changes in deformation in the FE model are more sharply expressed in the splitting of ray theory synthetic seismograms (Fig. 11), which correspond to infinite frequency waves. These data show an asymmetric variation in fast-polarization directions consistent with olivine CPO data. The gradual change of fast polarization directions in the North America Plate hinders a precise definition of the plate boundary width, but close to fault parallel polarizations are observed within ∼40 km from the plate boundary. In full-wave synthetic seismograms, which should be more representative of actual *SKS* waves that have dominant periods between 5 and 20 s, variations in both fast-polarization direction and delay time are smoother and the apparent plate boundary extent is broader (Figs 9 and 10). A 40-km-thick plate boundary deformation zone may however be retrieved by comparing fast-polarization direction profiles obtained using the multichannel analysis on waves with different dominant periods (Fig. 9).

SKS splitting measurements performed in central California using the S&C method show that the signature of the San Andreas transform fault system is only observed within 50 km of the plate boundary (Fig. 15). It is characterized by a 90° periodicity that indicates a variation with depth of the seismic anisotropy, which was modelled with a two-layer anisotropy model, with fast polarization directions parallel to the fault trend in the upper layer (e.g. Ozalaybey & Savage 1995; Bonnin *et al.* 2010). These observations are in relatively good agreement with the results of the model 'TDT60' that show that the seismic anisotropy related to the plate boundary deformation is recorded in a domain 40–50 km wide.

Pn waves anisotropy data (Hearn 1996; Buehler & Shearer 2010) and eikonal tomography (Lin *et al.* 2009) imply, on the other hand, that the strike-slip-related deformation beneath central California affects a broader region of the North America Plate, up to 150 km away from the plate boundary. A slightly broader strike-slip-related deformation zone in the lithospheric mantle beneath the North America Plate (60 km wide) is indeed predicted in our thermomechanical models, due to the asymmetry in the initial thermal structure of the two plates, but this is still a factor two lower than the width inferred from *Pn* and surface wave data. The broad strike-slip-related deformation zone inferred from these data is also not consistent with *SKS* splitting measurements performed beneath the Great Valley and Sierra Nevada that systematically show E-/W-trending fast-polarization directions and no significant backazimuthal variations (Ozalaybey & Savage 1995; Hartog & Schwartz 2000, 2001; Polet & Kanamori 2002; Bonnin *et al.* 2010; see Fig. 15). This discrepancy may result from a poor lateral resolution of surface waves data and by trade-offs between anisotropy and heterogeneity on *Pn* traveltimes.

The asymmetry in the strain rate distribution in the thermomechanical models (Fig. 3) results from the lateral variation of the initial geotherm, which is interpreted as caused by the opening of an asthenospheric window beneath coastal California in response to the northward migration of the Mendocino Triple Junction (Atwater 1970; Dickinson & Snyder 1979; Dickinson 1997). Since most of the stations are located on the North America Plate, we cannot test if this asymmetry is present or not in the San Andreas Fault system, but the lateral extent of the domain bearing a depth-dependent anisotropy east of the fault is consistent with a rather gradual change in deformation kinematics. Such a diffuse plate boundary is in accordance with the model proposed by Teyssier & Tikoff (1998) for the San Francisco Bay area. In the light of present results, one may also speculate that variations in the seismic anisotropy pattern along the plate boundary, such as the lack of fast polarization directions parallel to the plate boundary in southern California (Liu *et al.* 1995; Monteiller & Chevrot 2011), may record changes in the thermal structure of the plates.

4.3 Vertical resolution of teleseismic shear waves splitting data

In the present models, the plate boundary is characterized by a gradual variation of the orientation and strength of olivine CPO and hence of seismic anisotropy with depth (Figs 5 and 6). The maximum concentration of olivine [100] axes is always subhorizontal, but rotates from fault parallel to rather –45° from the fault plane with increasing depth. The maximum concentration of [010] axes, which is normal to the fault and subhorizontal in the lithospheric mantle, becomes dispersed in a vertical plane oriented at 45° from the strike of the plate boundary in the sublithospheric mantle (Fig. 6). The olivine CPO also decreases with depth (Fig. 5C). Fast quasi-shear waves polarization directions follow the rotation of the [100] maximum; the birefringence for a vertically propagating shear wave decreases with depth. The analysis of the splitting of synthetic shear waves propagating in this model allows therefore testing the power of these data to unravel gradual vertical variations in anisotropic properties.

Although gradual, the vertical changes in seismic properties inside the model induced, as expected, a backazimuthal variation of the splitting parameters with a 90° periodicity (Fig. 12). This variation is similar to the one classically interpreted in terms of two layers of anisotropy (Savage & Silver 1993). Nonetheless, our attempts to fit the modelled splitting observations using a two-layer anisotropic model produced models inconsistent with the crystallographic fabrics observed beneath the plate boundary. Based on this disagreement, we conclude that the fact that two-layer models consistently fit *SKS* splitting observations at 16 stations in the vicinity of the San Andreas Fault in central California (Bonnin *et al.* 2010) implies a much sharper transition between the lithosphere and the asthenosphere deformations in the natural system. Previous modelling of the San Andreas Fault zone seismic anisotropy by Savage *et al.* (2004) also supports this conclusion as the observed

backazimuthal variations of the splitting parameters in Northern California were only fitted by a model characterized by sharp variations in the directions of fast axis at depth associated with a strong viscosity contrast between the lithospheric and asthenospheric layers. *S*-to-*P* receiver functions studies of the lithosphere/asthenosphere boundary beneath California (Li 2007) tend to confirm this hypothesis, since a highly energetic pulse, in accordance with a sharp contrast in elastic properties, is observed close to the plate boundary.

5 CONCLUSION

We performed forward modelling to address the robustness of teleseismic shear wave splitting measurements to probe the vertical and lateral extent of the deformation beneath the Pacific/North America Plate boundary as well as the relation between the observed rotation of the fast-polarization directions with the westward migration of the plate boundary. Our approach combined thermomechanical modelling of a migrating strike-slip plate boundary, modelling of the CPO evolution and of the resulting 3-D elastic properties of the mantle, modelling of synthetic shear waves through this model and the measurement of shear wave splitting on these synthetics using different methods.

Among the different thermomechanical model configurations tested, *SKS* splitting data in central California are best fitted by a model with a hotter geotherm within 60 km of the plate boundary representing a thin lithosphere domain associated with the opening of an asthenospheric window due to the northward migration of the Mendocino Triple Junction. Comparison between *SKS* splitting data in the models and in central California shows that the westward motion of the plate boundary cannot explain the rotation of fast quasi-shear wave polarization directions observed east of the San Andreas Fault in central California, which probably records active flow in the asthenosphere as proposed by several previous studies.

The ability of the different synthetic approaches to localize horizontally and vertically the fault-related deformation differs significantly. Splitting measurements made on ray theory synthetics show an asymmetric variation in fast-polarization directions that closely follows the changes in olivine CPO in the input model. In contrast, analysis of splitting on full-wave synthetics, which take into account finite frequency effects and should therefore be more representative of actual *SKS* observations, results in smooth lateral variations of the anisotropic parameters. Despite strong variations in both intensity and orientation of anisotropy throughout the model, the location and width of the plate boundary can only be retrieved by comparing fast-polarization direction profiles obtained using the multichannel analysis on waves with different dominant periods. Indeed the density of broad-band stations is probably insufficient to attempt to image anisotropic structures from SI measurements, as Monteiller & Chevrot (2011) did in Southern California.

Vertical variations in anisotropy may only be investigated through individual splitting measurements. Such measurements performed on synthetics recorded at the plate boundary show a backazimuthal dependence of the splitting parameters with a 90° periodicity that is consistent with the vertical variation of the anisotropic properties in the model. Fitting these data with conventional two-layer models gives meaningful results, suggesting that this approach is not effective for analysing smooth vertical variations of anisotropy. As a consequence, we infer that the homogeneity of the two-layer models accounting for the observations in the vicinity of the San Andreas Fault indicates a sharp transition between lithospheric and asthenospheric deformations beneath this plate boundary.

ACKNOWLEDGMENTS

Thoughtful and constructive reviews were provided by Martha Kane Savage and an anonymous reviewer. Part of the research leading to these results has received funding from the European Research Council under the European Union's Seventh Framework Programme (FP7/2007–2013)/ERC Grant agreement 2404473 'CoMITAC'.

REFERENCES

Atwater, T., 1970. Implications of plate tectonics for the Cenozoic tectonic evolution of the Western North America, *Geol. Soc. Am. Bull.,* **81,** 3513–3536.

Bai, Q., Mackwell, S.J. & Kohlstedt, D.L., 1991. High-temperature creep of olivine single crystals, 1, mechanical results for buffered samples, *J. geophys. Res.,* **96,** 2441–2463.

Benz, H.M., Zandt, G. & Oppenheimer, D.H., 1992. Lithospheric structure of Northern California from teleseismic images of the upper mantle, *J. geophys. Res.,* **97,** 4791–4807.

Bonnin, M., Barruol, G. & Bokelmann, G.H.R., 2010. Upper mantle deformation beneath the North American-Pacific plate boundary in California from SKS splitting, *J. geophys. Res.,* **115,** B04307, doi:10.1029/2009JB006438.

Buehler, J.S. & Shearer, P.M., 2010. Pn tomography of the wester United States using USArray, *J. geophys. Res.,* **115,** doi:10.1029/2009JB006874.

Bunge, H.J., 1982. *Texture Analysis in Material Sciences: Mathematical Methods,* Butterworths, London, 583 p.

Burdick, S. *et al*., 2008. Upper mantle heterogeneity beneath North America from travel time tomography with global and USArray transportable array data, *Seismol. Res. Lett.,* **79,** 384–392, doi:10.1785/gssrl.79.3.384.

Chéry, J., Zoback, M.D. & Hassani, R., 2001. An integrated mechanical model of the San Andreas fault in central and northern California, *J. geophys. Res.,* **106,** 22 051–22 066, doi:10.1029/2001JB000382.

Chéry, J., Zoback, M.D. & Hickman, S., 2004. A mechanical model of the San Andreas fault and SAFOD pilot hole stress measurements, *Geophys. Res. Lett.,* **31,** doi:10.1029/2004GL019521.

Chevrot, S., 2000. Multichannel analysis of shear wave splitting, *J. geophys. Res.,* **105,** 21 579–21 590, doi:10.1029/2000JB900199.

Chevrot, S., 2006. Finite-frequency vectorial tomography: a new method for high-resolution imaging of the upper mantle anisotropy, *Geophys. J. Int.,* **165,** 641–657, doi:10.1111/j.1365-246X.2006.02982.x.

Chevrot, S., Favier, N. & Komatitsch, D., 2004. Shear wave splitting in three-dimensional anisotropic media, *Geophys. J. Int.,* **159,** 711–720, doi:10.1111/j.1365-246X.2004.02432.x.

Cundall, P.A. & Board, M., 1988. A microcomputer program for modelling large-strain plasticity problems, in *Proceedings of 6th International Conference in Numerical Methods in Geomechanics,* eds Swoboda, G. & Balkema, A.A., Brookfield, VT, pp. 2101–2108.

Dickinson, W.R., 1997. Tectonic implications of Cenozoic volcanism in coastal California, *Geol. Soc. Am. Bull.,* **109,** 936–954.

Dickinson, W.R. & Snyder, W.S., 1979. Geometry of the subducted slabs related to the San Andreas transform, *J. Geol.,* **87,** 609–627.

Favier, N. & Chevrot, S., 2003. Sensitivity kernels for shear wave splitting in transverse isotropic media, *Geophys. J. Int.,* **153,** 213–228, doi:10.1046/j.1365-246X.2003.01894.x.

Fontaine, F.R., Barruol, G., Tommasi, A. & Bokelmann, G.H.R., 2007. Upper mantle flow beneath French Polynesia from shear-wave splitting, *Geophys. J. Int.,* **170,** 1262–1288, doi:10.1111/j.1365-246X.2007.03475.x.

Gripp, A.E. & Gordon, R.B., 2002. Young tracks of hotspots and current plate velocities, *Geophys. J. Int.,* **150,** 321–361, doi:10.1046/j.1365-246X.2002.01627.x.

Hammond, J.O.S., Kendall, J.M., Angus, D. & Wookey, J., 2010. Interpreting spatial variations in anisotropy: insights into the Main Ethiopian Rift from SKS waveform modelling, *Geophys. J. Int.,* doi:10.1111/j.1365-246X.2010.04587.x.

Harmon, N., Forsyth, D.A. & Fischer, K.M., 2004. Variations in shear wave splitting in young Pacific seafloor, *Geophys. Res. Lett.,* **31,** doi:10.1029/2004GL020495.

Hartog, R. & Schwartz, S., 2000. Subduction-induced strain in the upper mantle east of the Mendocino triple junction, California, *J. geophys. Res.,* **105,** 7909–7930, doi:10.1029/1999JB900422.

Hartog, R. & Schwartz, S., 2001. Depth-dependent mantle anisotropy below the San Andreas fault system: apparent splitting parameters and waveforms, *J. geophys. Res.,* **106,** 4155–4167, doi:10.1029/2000JB900382.

Hassani, R., Jongmans, D. & Chéry, J., 1997. Study of plate deformation and stress in subduction processes using two-dimensional numerical models, *J. geophys. Res.,* **102,** 17 951–17 965, doi:10.1029/97JB01354.

Hearn, T.M., 1996. Anisotropic Pn tomography in the western United States, *J. geophys. Res.,* **101,** 8403–8414, doi:10.1029/96JB00114.

Hess, H.H., 1964. Seismic anisotropy of the uppermost mantle under oceans, *Nature,* **203,** 629–631.

Komatitsch, D. & Tromp, J., 1999. Introduction to the spectral-element method for 3-D seismic waves propagation, *Geophys. J. Int.,* **139,** 806–822, doi:10.1046/j.1365-246x.1999.00967.x.

Lachenbruch, A.H. & Sass, J.H., 1980. Heat flow and energetics of the San Andreas Fault Zone, *J. geophys. Res.,* **85,** 6185–6222.

Lachenbruch, A.H., Sass, J.H. & Galanis, S.P., 1985. Heat-flow in the southernmost California and the origin of the Salton Trough, *J. geophys. Res.,* **90,** 6709–6736.

Lebensohn, R.A. & Tomé, C.N., 1993. A self-consistent anisotropic approach for the simulation of plastic deformation and texture development of polycrystals: application to zirconion alloys, *Acta. Metall. Mater.,* **41,** 2611–2624, doi:10.1016/0956-7151(93)90130-K.

Li, X., 2007. The lithosphere-asthenosphere boundary beneath the western United States, *Geophys. J. Int.,* **170,** 700–710, doi:10.1111/j.1365-246X.2007.03428.x.

Lin, F.C., Ritzwoller, M.H. & Snieder, R., 2009. Eikonal tomography: surface wave tomography by phase-front tracking across a regional broadband seismic array, *Geophys. J. Int.,* **177,** 1091–1110, doi:10.1111/j.1365-246X.2009.04105.x.

Liu, H.L., Davis, P.M. & Gao, S., 1995. SKS splitting beneath southern California, *Geophys. Res. Lett.,* **22,** 767–770, doi:10.1029/95GL00487.

Mainprice, D., 1990. A FORTRAN program to calculate seismic anisotropy from the lattice preferred orientation of minerals, *Comput. Geosci.,* **16,** 385–393.

Mainprice, D., Tommasi, A., Couvy, H. & Cordier, P., 2005. Pressure sensitivity of olivine slip systems and seismic anisotropy of earth's upper mantle, *Nature,* **433,** 731–733, doi:10.1038/nature 03266.

Monteiller, V. & Chevrot, S., 2010. How to make robust splitting measurements for single-station analysis and three-dimensional imaging of seismic anisotropy, *Geophys. J. Int.,* **182,** 311–328.

Monteiller, V. & Chevrot, S., 2011. High-resolution imaging of the deep anisotropic structure of the San Andreas Fault system beneath southern California, *Geophys. J. Int.,* **182,** 418–446, doi:10.1111/j.1365-246X.2011.05082.x.

Ozalaybey, S. & Savage, M.K., 1994. Double-layer anisotropy resolved from *S* phases, *Geophys. J. Int.,* **117,** 653–664, doi:10.1111/j.1365-246X.1994.tb02460.x.

Ozalaybey, S. & Savage, M.K., 1995. Shear wave splitting beneath the western United States in relation to plate tectonics, *J. geophys. Res.,* **100,** 18 135–18 149, doi:10.1029/95JB00715.

Polet, J. & Kanamori, H., 2002. Anisotropy beneath California: shear wave splitting measurements using a dense broadband array, *Geophys. J. Int.,* **149,** 313–327, doi:10.1046/j.1365-246X.2002.01630.x.

Savage, M.K., 1999. Seismic anisotropy and mantle deformation: what have we learned from shear wave splitting? *Rev. Geophys.,* **37,** 65–106, doi:10.1029/98RG02075.

Savage, M.K. & Silver, P.G., 1993. Mantle deformation and tectonics: constraints from seismic anisotropy in western United States, *Phys. Earth planet. Inter.,* **78,** 207–227.

Savage, M., Fisher, K.M. & Hall, C.E., 2004. Strain modelling, seismic anisotropy and coupling at strike-slip boundaries: application in New Zealand and the San Andreas fault, *Geol. Soc. Lond., Spec. Publ.,* **227,** 9–39.

Savage, M.K., Tommasi, A., Ellis, S. & Chéry, J., 2007. Modeling strain and anisotropy along the Alpine fault, South Island, New Zealand, in *A Continental Plate Boundary: Tectonics at South Island, New Zealand,* Vol. 175, pp. 289–305, eds Okaya, D., Stern, T. & Davey, F., American Geophysical Union, Geophysical Monograph Series.

Silver, P.G., 1996. Seismic anisotropy beneath the continents: probing the depths of geology, *Annu. Rev. Earth planet. Sci.,* **24,** 385–432.

Silver, P.G. & Chan, W.W., 1991. Shear wave splitting and subcontinental mantle deformation, *J. geophys. Res.,* **96,** 16 429–16 454, doi:10.1029/91JB00899.

Silver, P.G. & Holt, W.E., 2002. The mantle flow field beneath western North America, *Science,* **295,** 1054–1057.

Silver, P.G. & Savage, M.K., 1994. The interpretation of shear-wave splitting parameters in the presence of two anisotropic layers, *Geophys. J. Int.,* **119,** 949–963, doi:10.1111/j.1365-246X.1994.tb04027.x.

Teanby, N.A., Kendall, J.M. & van der Baan, M., 2004. Automation of shear-wave splitting measurements using cluster analysis, *Bull. seism. Soc. Am.,* **94,** 453–463.

Teyssier, C. & Tikoff, B., 1998. Strike-slip partitioned transpression of the San Andreas fault system: a lithospheric-scale approach, *Geol. Soc. Lond., Spec. Publ.,* **135,** 143–158.

Titus, S.J., Medaris, L.G., Wang, H.F. & Tikoff, B., 2007. Continuation of the San Andreas fault system into the upper mantle: evidence from spinel peridotite xenoliths in the Coyote Lake basalt, central California, *Tectonophysics,* **429,** 1–20, doi:10.1016/j.tecto.2006.07.004.

Tommasi, A., 1998. Forward modeling of the development of seismic anisotropy in the upper mantle, *Earth planet. Sci. Lett.,* **160,** 1–13, doi:10.1016/S0012-821X(98)00081-8.

Tommasi, A., Tikoff, B. & Vauchez, A., 1999. Upper mantle tectonics: three-dimensionnal deformation, olivine crystallographic fabrics and seismic properties, *Earth planet. Sci. Lett.,* **168,** 173–186, doi:10.1016/S0012-821X(99)00046-1.

Tommasi, A., Mainprice, D., Canova, G. & Chastel, Y., 2000. Viscoplastic self-consistent and equilibrium-based modeling of olivine lattice preferred orientations. Implications for the upper mantle seismic anisotropy, *J. geophys. Res.,* **105,** 7893–7908, doi:10.1029/1999JB900411.

Turcotte, D.L. & Schubert, G., 1982. *Geodynamics: Application of Continuum Physics to Geological Problems,* John Wiley & Sons, New York.

Vauchez, A., Tommasi, A. & Mainprice, D., 2012. Faults (shear zones) in the Earth's mantle, *Tectonophysics,* **558–559**, 1–27, doi:10.1016/j.tecto.2012.06.006.

Wenk, H.R., Bennett, K., Canova, G.R. & Molinari, A., 1991. Modelling plastic deformation of peridotite with the self-consistent theory, *J. geophys. Res.,* **96,** 8337–8349.

Wolfe, C. & Silver, P.G., 1998. Seismic anisotropy of oceanic upper mantle: shear wave splitting methodologies and observations, *J. geophys. Res.,* **103,** 749–771.

Wolfe, C.J. & Solomon, S.C., 1998. Shear wave splitting and implication for mantle flow beneath the MELT region of the East Pacific Rise, *Science,* **280,** 1230–1232.

Wüstefeld, A. & Bokelmann, G.H.R., 2007. Null detection in shear-wave splitting measurements, *Bull. seism. Soc. Am.,* **97,** 1204–1211.

Wüstefeld, A., Al-Harrasi, O., Verdon, J., Wookey, J. & Kendall, J.M., 2010. A strategy for automated analysis of passive microseismic data to image seismic anisotropy and fracture characteristics, *Geophys. Prospect.,* **58,** 755–773, doi:10.1111/j.1365-2478.2010.00891.x.